

2

AD-A261 065



Interaction of O₂ with the Fe_{.84}Cr_{.16} (001) Surface Studied by Photoelectron Spectroscopy

Prepared by

J. R. LINCE and S. V. DIDZIULIS
Mechanics and Materials Technology Center
Technology Operations
The Aerospace Corporation

and

D. K. SHUH, T. D. DURBIN, and J. A. YARMOFF
Department of Physics
University of California, Riverside

15 July 1992

Prepared for

SPACE AND MISSILE SYSTEMS CENTER
AIR FORCE MATERIEL COMMAND
Los Angeles Air Force Base
P. O. Box 92960
Los Angeles, CA 90009-2960

DTIC
SELECT
FEB 16 1993
S B D

Engineering and Technology Group

THE AEROSPACE CORPORATION
El Segundo, California

93 2 12 163

APPROVED FOR PUBLIC RELEASE:
DISTRIBUTION UNLIMITED

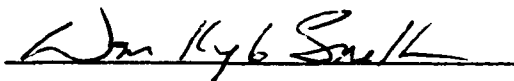
93-02845



This report was submitted by The Aerospace Corporation, El Segundo, CA 90245-4691, under Contract No. F04701-88-C-0089 with the Space and Missile Systems Center, P. O. Box 92960, Los Angeles, CA 90009-2960. It was reviewed and approved for The Aerospace Corporation by R. W. Fillers, Principal Director, Mechanics and Materials Technology Center. Capt. M. W. Borden was the project officer for the Mission-Oriented Investigation and Experimentation (MOIE) program

This report has been reviewed by the Public Affairs Office (PAS) and is releasable to the National Technical Information Service (NTIS). At NTIS, it will be available to the general public, including foreign nationals.

This technical report has been reviewed and is approved for publication. Publication of this report does not constitute Air Force approval of the report's findings or conclusions. It is published only for the exchange and stimulation of ideas.



W. KYLE SNEDDON, Captain, USAF
MOIE Program Manager



MARK W. BORDEN, Captain, USAF
SSUSI/SSULI Project Officer

UNCLASSIFIED

SECURITY CLASSIFICATION OF THIS PAGE

REPORT DOCUMENTATION PAGE

1a. REPORT SECURITY CLASSIFICATION Unclassified		1b. RESTRICTIVE MARKINGS	
2a. SECURITY CLASSIFICATION AUTHORITY		3. DISTRIBUTION/AVAILABILITY OF REPORT Approved for public release; distribution unlimited	
2b. DECLASSIFICATION/DOWNGRADING SCHEDULE			
4. PERFORMING ORGANIZATION REPORT NUMBER(S) TR-92(2935)-10		5. MONITORING ORGANIZATION REPORT NUMBER(S) SMC-TR-93-02	
6a. NAME OF PERFORMING ORGANIZATION The Aerospace Corporation Technology Operations	6b. OFFICE SYMBOL <i>(If applicable)</i>	7a. NAME OF MONITORING ORGANIZATION Space and Missile Systems Center	
6c. ADDRESS (City, State, and ZIP Code) El Segundo, CA 90245-4691		7b. ADDRESS (City, State, and ZIP Code) Los Angeles Air Force Base Los Angeles, CA 90009-2960	
8a. NAME OF FUNDING/SPONSORING ORGANIZATION	8b. OFFICE SYMBOL <i>(If applicable)</i>	9. PROCUREMENT INSTRUMENT IDENTIFICATION NUMBER F04701-88-C-0089	
8c. ADDRESS (City, State, and ZIP Code)		10. SOURCE OF FUNDING NUMBERS	
		PROGRAM ELEMENT NO.	PROJECT NO.
		TASK NO.	WORK UNIT ACCESSION NO.
11. TITLE (Include Security Classification) Interaction of O₂ with the Fe₈₄Cr₁₆(001) Surface Studied by Photoelectron Spectroscopy			
12. PERSONAL AUTHOR(S) Lince, Jeffrey R., Didziulis, Stephen V., Shuh, D. K., Durbin, T. D., and Yarmoff, J. A.			
13a. TYPE OF REPORT	13b. TIME COVERED FROM _____ TO _____	14. DATE OF REPORT (Year, Month, Day) 1992 July 15	15. PAGE COUNT 39
16. SUPPLEMENTARY NOTATION			
17. COSATI CODES			18. SUBJECT TERMS (Continue on reverse if necessary and identify by block number) Oxidation, Steels, Photoelectron spectroscopy, Synchrotron radiation, Alloy surfaces
FIELD	GROUP	SUB-GROUP	
19. ABSTRACT (Continue on reverse if necessary and identify by block number) The surface oxidation of a steel-like alloy was investigated to help determine how the efficiency of lubricant additives such as lead naphthenate might be affected by the chemical state of a high-Cr steel bearing surface. Soft X-ray photoelectron spectroscopy (SXPS; $h\nu = 130 - 600$ eV) employing synchrotron radiation and X-ray photoelectron spectroscopy (XPS; $h\nu = 1486.6$ eV) employing Al-K α X rays were used to study the effect of molecular oxygen adsorption (1 to 10^4 L, where $1\text{L} \equiv 10^{-6}$ Torr-sec) on the (001) surface of Fe ₈₄ Cr ₁₆ at room temperature. The use of multiple photon energies allowed a qualitative determination of the distribution of species in the oxide film perpendicular to the surface. Prior to oxidation, Fe ₈₄ Cr ₁₆ samples were annealed to different temperatures to produce varying concentrations of Cr in the top few monolayers of the (001) surface. The differences between the oxide films produced on these different surfaces were determined with SXPS using primarily the Fe 3p, Cr 3p, and valence levels. Small amounts of carbidic carbon (≤ 1 monolayer) that had segregated to the (001) surface of the Fe ₈₄ Cr ₁₆ alloy during initial sputter/anneal treatments were removed during the first ~ 5 L O ₂ exposure. In general, the resistance of the Fe ₈₄ Cr ₁₆ (001) surface to oxidation was directly related to the initial Cr concentration at the surface. The oxide films were richer in Cr compared to the			
20. DISTRIBUTION/AVAILABILITY OF ABSTRACT <input checked="" type="checkbox"/> UNCLASSIFIED/UNLIMITED <input type="checkbox"/> SAME AS RPT. <input type="checkbox"/> DTIC USERS		21. ABSTRACT SECURITY CLASSIFICATION Unclassified	
22a. NAME OF RESPONSIBLE INDIVIDUAL		22b. TELEPHONE (Include Area Code)	22c. OFFICE SYMBOL

UNCLASSIFIED

SECURITY CLASSIFICATION OF THIS PAGE

bulk concentration for the lowest O₂ exposures, and became increasingly enriched in Fe for increasing exposures, in agreement with studies by other groups. The resulting mixed Fe-Cr-O film contained Cr in the form of Cr³⁺ for all exposures. The Fe was in the form of Fe²⁺ and Fe³⁺, with an increasing Fe³⁺/Fe²⁺ ratio as O₂ exposure is increased. The results indicate that for O₂ exposures < 10⁴L, the oxide films do not exhibit sharp boundaries between the Cr-rich and Fe-rich layers, in contrast to previously reported results for much larger (i.e. atmospheric) exposures. The observation of a mixed film, along with thermodynamic analysis, low-energy electron diffraction results, and comparison with other studies is consistent with an oxide film consisting of appreciable amounts of an amorphous, Fe_{1+x}Cr_{2-x}O₂-like species. The concentration of Fe_{1+x}Cr_{2-x}O₄ at the films' surfaces decreased in favor of Fe₂O₃ as the O₂ exposure level increased.

These results indicate that the antiwear ability of lead naphthenate is dependent on surface preparation procedures of a high-Cr steel (e.g., 440C) bearing. In addition, the results indicate that very small residual O₂ gas pressures in the space environment could produce thin oxide films that would interfere with the formation of a protective Pb film from decomposition of the lead naphthenate.

UNCLASSIFIED

SECURITY CLASSIFICATION OF THIS PAGE

PREFACE

This work was supported predominantly by Air Force Systems Command, Space Systems Division under Contract No. F04701-88-C-0089. Research was carried out partly at the National Synchrotron Light Source (NSLS), Brookhaven National Laboratory, which is supported by the U.S. Department of Energy, Division of Materials Sciences and Division of Chemical Sciences (DOE Contract No. DE-AC02-76CH00016). The authors gratefully acknowledge the staff at NSLS for their assistance and C. Uebing of the University of Chicago for the generous gift of several Fe_{.84}Cr_{.16} samples. In addition, we thank P.D. Fleischauer and P.A. Bertrand for helpful comments.

DTIC QUALITY INSPECTED 3

Accession For	
NTIS GRA&I	<input checked="" type="checkbox"/>
DTIC TAB	<input type="checkbox"/>
Unannounced	<input type="checkbox"/>
Justification	
By _____	
Distribution/	
Availability Codes	
Dist	Avail and/or Special
A-1	

CONTENTS

1.	INTRODUCTION.....	7
2.	EXPERIMENTAL.....	9
3.	RESULTS.....	13
3.1	XPS USING Al K α X-RAYS - ANALYSIS THROUGH THE ENTIRE DEPTH OF THE FILM	13
3.2	SOFT X-RAY PHOTOELECTRON SPECTROSCOPY (SXPS) - ANALYSIS OF THE SURFACE OF THE OXIDE FILM.....	17
3.2.1	SXPS Core Levels.....	17
3.2.2	Energy Variation of SXPS Core Levels.....	21
3.2.3	SXPS Valence Band Spectra	23
3.2.4	Variation of Surface Concentrations During O ₂ Exposure.....	24
4.	DISCUSSION.....	31
5.	SUMMARY.....	35
6.	REFERENCES.....	37

FIGURES

1. XPS spectra of the Fe $2p_{3/2}$ and Cr $2p_{3/2}$ core levels after exposure to O ₂	14
2. Variation of Fe:Cr and oxide:metal ratios as a function of O ₂ exposure, determined from XPS core levels.....	15
3. Difference in the binding energies of the oxide and metal contributions from XPS, shown for the Fe $2p_{3/2}$ and the Cr $2p_{3/2}$ peaks.....	16
4. Full-widths-at-half-maximum (FWHM) for the deconvolved Fe-oxide and Cr-oxide XPS peaks ($2p_{3/2}$ core levels).....	17
5. Fe 3p and Cr 3p core levels for the R = 2.9 surface	19
6. Fe 3p and Cr 3p core levels for the R = 10.5 surface	20
7. Results of deconvolution by least-squares fitting of the high KE (hv = 220 eV) Fe 3p and Cr 3p core-level spectra to a combination of an oxide and a metallic peak.....	22
8. Difference in the oxide and metal 3p peak BEs determined by deconvolution of the SXPS core levels taken of the R = 10.5 surface.....	23
9. Valence band spectra of the R = 10.5 surface taken with hv = 154 and 254 eV.....	24
10. Cr _{oxide} :Cr _{metal} ratios for the three surfaces studied by SXPS.....	25
11. Fe _{oxide} :Fe _{metal} ratios for the three surfaces studied by SXPS.....	26
12. The high KE Fe _{oxide} :Fe _{metal} ratios divided by the same ratios determined from low KE data	27
13. Fe _{total} :Cr _{total} [(Fe _{oxide} +Fe _{metal})/(Cr _{oxide} +Cr _{metal})] ratios for the three surfaces studied by SXPS	28
14. Fe _{oxide} :Cr _{oxide} ratios for the three surfaces studied by SXPS.....	29
15. The high KE Fe _{oxide} :Cr _{oxide} ratio divided by the same ratio determined from low KE data	30
16. Schematic representation of results in this study on oxide film formation on the Fe ₈₄ Cr ₁₆ (001) surface after exposure to O ₂ (≤ 10,000 L O ₂) at room temperature	34

TABLES

1 Photoelectron Kinetic Energies and Corresponding Inelastic Mean Free Paths (IMFP) Used in This Study.....	11
2. Binding Energies of $\text{Fe}_{1+x}\text{Cr}_{2-x}\text{O}_4$ Spinels	32

1. INTRODUCTION

The interactions of antiwear and extreme-pressure lubricant additives with surfaces of steel bearings are related to the chemical bonding of the additive molecules to the steel surface. In order to understand this interaction, it is necessary to determine the composition and structure in the top-most few nanometers of the steel surface. For example, the use of the extreme-pressure additive lead naphthenate (PbNp) with bearings made of 440C steel (a high-Cr steel) in space systems requires knowledge of the chemical makeup of the oxide film formed on the bearing surface at approximately room temperature. For this system, the interaction between PbNp and the 440C steel surface depended strongly on preparation conditions.¹

The oxidation behavior of the surfaces of high-Cr steels and steel-like Fe-Cr alloys has been studied extensively for both dry (air/O₂) and aqueous environments.² Studies in air or O₂, however, have concentrated on oxidation of steels at elevated temperatures (see, for example, Refs. 3 - 8), while few have examined the oxidation at room temperature.⁹⁻¹²

For oxidation at temperatures $\leq 600^\circ\text{C}$, it is believed that the oxide film formed after atmospheric exposure consists of a Cr-rich layer primarily composed of Cr₂O₃ at the oxide/metal interface and a layer consisting of primarily Fe₂O₃ that forms on top of the Cr-rich layer.¹ Some studies have also indicated that iron chromite (FeCr₂O₄) forms at the interface between the Cr₂O₃ and Fe₂O₃ layers. This duplex structure is apparently the result of the relative thermodynamic stability of Cr₂O₃ (compared to the iron oxides),¹³ resulting in Cr₂O₃ formation at low O₂ exposures. After formation of a diffusion barrier layer at higher O₂ exposures, only the more mobile Fe atoms can diffuse through the oxide film.¹⁴⁻¹⁶ Eventually, the thickness of the oxide film prevents further oxidation. The Cabrera-Mott theory¹⁷ suggests that oxide film formation is caused by the electric field produced between the adsorbed oxygen anions at the oxide film surface and the metal cations at the oxide/metal interface. As the oxide film thickness increases, the field decreases, the activation barrier for diffusion increases, and the oxide film growth rate becomes negligible.

Experimentation in the low O₂ exposure regime could help to elucidate the details of this "thermodynamic-to-kinetic transition" in the growth of oxide films on steels. In addition, the formation of oxide films on bearing surfaces in the low-pressure space environment corresponds to a low O₂ exposure regime. However, few studies of low O₂ exposures have been conducted, especially at room temperature. Leygraf, et al., studied Fe_{.84}Cr_{.16} (001) and (011) surfaces with Auger electron spectroscopy (AES) and low-energy electron diffraction (LEED) after oxidation with 0.1 to 100 Langmuirs (L) of O₂.¹⁰ Their results indicated that the initial reaction resulted primarily in the formation of a Cr-O overlayer. Continued O₂ exposure resulted in the formation of an Fe-O overlayer on top of the initial Cr-rich layer. No detailed information concerning the exact chemical states in the oxide film was presented. Olefjord studied the interaction of O₂ with the surfaces of polycrystalline Fe-Cr alloys (with 6 to 20% Cr) using X-ray photoelectron spectroscopy (XPS),⁹ which is more sensitive to chemical state changes than AES. However, that study was conducted for large exposures of O₂, i.e., close to atmospheric exposure.

We have conducted a detailed study of the interaction of O₂ with the Fe_{.84}Cr_{.16} (001) surface in the low-exposure regime (1 to 10,000 L O₂) at room temperature. Variable photon energy soft X-ray

photoelectron spectroscopy (SXPS) and XPS provided information on the oxidation mechanism and chemical species present in the oxide film. The use of several photon energies resulted in a wide variation of kinetic energies (KE) of the emitted photoelectrons. Since the depth probed by photoelectron spectroscopy depends on the photoelectron KE, we were able to develop a "qualitative depth profile" of Fe and Cr in the oxide film. Determination of the positions of the core-level peaks and analysis of the shape of the valence band spectra allowed us to ascertain which chemical species are present in the oxide film, especially in the top 3 to 5 Å of the surface region. In addition, we have taken advantage of the observation that the Fe:Cr ratio at the surface of an unoxidized Fe-Cr alloy depends on annealing conditions. As a result, the effect of different initial Cr surface concentrations on the chemical state of the oxide film could be elucidated.

Our results show that increasing amounts of Cr segregation to the surface of the unoxidized Fe₈₄Cr₁₆ (001) sample inhibited oxide film formation during exposure to O₂. Submonolayer amounts of carbidic carbon on the unoxidized surface were oxidized and removed by exposures ≤ 5 L O₂. For all exposures ≤ 10,000 L O₂, the entire depth of the oxide film consisted of mixed Fe-Cr-O species. The films produced at low exposures were enhanced in Cr (compared to the Fe:Cr ratio in the bulk alloy), while the Fe was present predominantly as Fe²⁺. Increasing O₂ exposure resulted in an increase in both the Fe:Cr and Fe³⁺/Fe²⁺ ratios in the oxide film.

2. EXPERIMENTAL

The ferritic Fe-Cr single-crystal alloy used in this study was grown using the Bridgeman method with a Cr concentration of 15 wt-% (corresponding to 16 at-%). Bulk impurities were present as follows: ~ 15 wt-ppm N, ~ 10 wt-ppm C, and ~ 10 wt-ppm S. The crystal was cut by spark erosion to ~ 1-mm thickness with its front and back faces approximately normal to the (001) plane.¹⁸ It was then polished to within 0.5° of the (001) plane using an abrasive slurry of alumina in ethanol (successively smaller grit sizes were used in the order 5.0, 0.3, then 0.05 μm). A back-reflection Laue X-ray photograph was characteristic of a crystalline bcc alloy, while X-ray rocking curve analysis of the (001) diffraction peak showed a small mosaic spread ($\leq 0.2^\circ$). Before installation in the two different vacuum systems, the sample was always rinsed in ethanol and dried in N_2 gas.

The XPS experiment was conducted in an ultra-high vacuum (UHV) system that consisted of two analytical chambers (only the one with XPS capability was used in this experiment), a sample treatment chamber, and a sample distribution chamber that allowed transfer between the various chambers without exposure to atmosphere. The analytical and treatment chambers are both ion- and titanium-sublimation-pumped, while the distribution chamber is ion-pumped. Base pressures for the analytical, treatment, and distribution chambers were 5×10^{-11} Torr, 1×10^{-10} Torr, and 1×10^{-10} Torr, respectively. Oxygen exposure was conducted in the sample treatment chamber by turning off the pumps, followed by leaking in 99.999% purity O_2 gas until a pressure in the range 10^{-7} to 10^{-5} Torr was reached for an appropriate time to give a 1 to 10,000 L exposure. The sample was turned away from the ion gauge filament during oxygen exposure to avoid effects due to atomic oxygen. After each exposure, the sample was transferred into the analysis chamber, which was equipped with a Surface Science Instruments XPS system (Model 301 X-probe) that had a focussed, monochromatized X-ray source (Al-K α X-rays; $h\nu = 1486.6$ eV). The system had a heating stage so that samples could be annealed before analysis. The temperatures attained were highly repeatable, but accurate only to within $\pm 25^\circ\text{C}$. For the individual core-level spectra, an X-ray spot size of 300 μm and an analyzer pass energy of 50 eV were used. These parameters gave a full-width-at-half-maximum (FWHM) of 0.88 eV for the Au $4f_{7/2}$ peak of a clean Au foil. Binding energies were determined relative to the Au $4f_{7/2}$ peak at 83.9 eV acquired from a clean Au foil. The electron takeoff angle could be changed by rotating the sample holder and was set 60° away from surface normal except where explicitly noted (the analyzer had a large angular cone of acceptance, i.e., $\sim 30^\circ$ wide). The core-level spectra were deconvolved into peaks composed of sums of Gaussian and Lorentzian functions, as discussed later in this section. Atomic percentages were calculated from Scofield sensitivity factors.¹⁹

The sample was subjected to multiple cycles of 1 keV Ar^+ -bombardment followed by annealing to 700°C (total bombardment time ~ 4 hours). For the XPS experiment, the surface was determined to have $\sim 6\%$ oxygen (in the form of oxidized iron and oxidized chromium) and 7% carbon (in carbidic form) within the XPS analysis depth (i.e., within an effective escape depth of $\lambda \cos 60^\circ \cong 9 \text{ \AA}$ ^{20,21}). A Princeton Research Instruments LEED system gave a sharp (001)- 1×1 pattern before oxygen exposure.

SXPS was conducted at beam line UV-8b at the National Synchrotron Light Source at Brookhaven National Laboratory. The electron spectrometer,²² monochromator,²³ and sample preparation/dosing chamber²⁴ have been described previously. The design of the angle-integrating electron spectrometer is based on an electrostatic ellipsoidal mirror, which allows electron collection over a solid angle of $\sim \pi/2$ steradians, centered approximately about the sample normal. The relative intensity of the monochromatized synchrotron radiation was determined by measuring the total current resulting from the electron emission from the (carbon-contaminated) Au-coated final focussing mirror with an electrometer. The spectra were normalized by dividing the photoelectron signal by the photon intensity determined in this manner to cancel the effects of beam current variation. The resolution of the system (including contributions from the analyzer and monochromator) was estimated to be 0.4 eV at $h\nu = 120\text{-}250$ eV, 0.5 eV at $h\nu = 364$ eV, and 0.7 eV at $h\nu = 600$ eV. Wide scans taken at $h\nu = 600$ eV employed a resolution of ~ 1.2 eV.

For the SXPS experiments, the sample was subjected to cycles of bombardment with 1 keV Ar^+ ions (current density $\sim 1.0 \mu\text{A}/\text{cm}^2$) and heating at $\sim 700^\circ\text{C}$ in 1×10^{-7} Torr O_2 to remove segregated impurities. After several of these cycles, the final step involved bombardment with 1 keV followed by 0.5 keV Ar^+ ions, followed by a final anneal in the sample preparation chamber in UHV. Oxidation was studied on three surfaces that were prepared before O_2 exposure by heating to 600°C , 775°C , and 800°C , respectively, in the final anneal step. The sample temperatures were allowed to fall to $\sim 25^\circ\text{C}$ within ~ 1 min after the anneal. No oxygen was detected on the surfaces after this process, although 0.5 - 0.7 monolayers (ML) of carbidic carbon remained on the surfaces (the carbon film thickness is determined in Section 3.2.1). The temperature of this final anneal step and the cool-down rate determined the $\text{Fe}_{\text{total}}:\text{Cr}_{\text{total}}$ ratio at the surface of the unoxidized sample. However, the cool-down rate was not explicitly controlled in this study. The temperature of the sample during heating was measured using a near-IR pyrometer; the sample was sighted through a sapphire window. This method was considered accurate to within 40°C , but reproducible within $\pm 5^\circ\text{C}$. The relative atomic concentrations were determined using photoelectron cross sections tabulated by Yeh and Lindau.²⁵ A Microscience rear-view LEED system gave sharp (001)- 1×1 patterns for all the unoxidized surfaces, similar to the ones obtained before the XPS experiment.

Oxygen dosing at NSLS was performed by leaking nominally 99.999% O_2 into the preparation chamber. During O_2 exposure, the gate valve on a turbomolecular pump was throttled so that an equilibrium pressure of 10^{-7} to 10^{-5} Torr was maintained. The sample was not in line-of-sight of the ion gauge filament during exposure.

The wide range of photon energies (i.e., $h\nu = 130$ to 1486.6 eV) and therefore, KEs used in this study resulted in a range of surface sensitivities. Table 1 shows the KEs and calculated inelastic mean free paths (IMFP)^{20,21} of the various core and valence peaks used. The resultant range of IMFP values (i.e., 3.5 to 12 Å) allowed us to determine a "qualitative depth profile" of species in the near-surface region.

Table 1. Photoelectron Kinetic Energies and Corresponding Inelastic Mean Free Paths (IMFP) Used in This Study^a

Peak Designation	Kinetic Energy (eV)	IMFP (Å)		
SXPS:	Low KE Fe 3p Low KE Cr 3p C 1s O 1s	80	3.5	
	Low KE valence band	154	5.2	
	High KE Fe 3p High KE Cr 3p	170	5.5	
	High KE valence band	254	7.0	
	C 1s (Wide scan)	320	8.4	
	Fe 3p Cr 3p (Wide scan)	560	12.0	
	XPS:	Fe 2p	780	7.5
		Cr 2p	910	8.5
		O 1s	956	9.0

a. Determined from results in Refs. 20 and 21. Calculated values for metallic and oxide materials were similar (i.e., $\pm 0.1\text{Å}$) over this range of kinetic energies.

The Fe and Cr 3p spectra were deconvolved into metallic and oxide components using a peak-fitting procedure similar to that used for XPS, except that Voigt functions (approximated by Gaussian quadrature) were used instead of sums of Gaussians and Lorentzians. The asymmetric, or Doniach-Sunjic lineshape of the metallic Fe 3p peaks (as well as the contribution from the two spin-orbit split components) were simulated by using two Voigt functions with different Gaussian and Lorentzian widths to fit the unexposed surface. The shape of the resultant asymmetric peak was kept constant for metallic Fe 3p peaks at all oxygen exposures. The same procedure was used for the metallic Cr 3p peaks. The use of two peaks to simulate the metallic core-level shape was also applied to the metallic components of the Fe and Cr 2p_{3/2} XPS spectra.

The identifications of the oxides present in the surface region were made primarily by determining their binding energy (BE) shifts from the metallic components [defined as $\Delta_{BE} \equiv (\text{oxide BE}) - (\text{metallic BE})$] since the metallic positions remained virtually invariant ($\pm 0.05\text{ eV}$) before and after

oxidation. The literature references we chose to identify FeO and Fe₂O₃ also reported spectra for metallic Fe, and those chosen to identify Cr₂O₃ also reported spectra for metallic Cr. In this manner, problems with different referencing methods could be circumvented. The only exception is the identification of mixed oxides with compositions Fe_{1+x}Cr_{2-x}O₄ (0 ≤ x ≤ 1.4) from a study by Allen and coworkers¹⁴ in which Fe₂O₃ and Cr₂O₃ were also studied. The Δ_{BE} values of these mixed oxides were determined by taking the difference of their BE and the Fe₂O₃ (or Cr₂O₃) BE from Ref. 14 and then adding this to the Δ_{BE} of Fe₂O₃ (or Cr₂O₃) taken from other references.

3. RESULTS

This section is organized as follows: Section 3.1 presents the XPS results on the Fe and Cr 2p_{3/2} core levels, which are used to determine the chemical state throughout the depth of the oxide film. Section 3.2 presents the SXPS results, which represent the composition of the outer surface [i.e., the top 1 to 3 monolayers (ML)]. The Fe and Cr 3p core-level spectra are presented in Section 3.2.1, analysis of the energy positions of the Fe and Cr 3p core levels is presented in Section 3.2.2, valence band spectra are shown in Section 3.2.3, and a determination of surface concentrations for samples with different initial surface Fe:Cr ratios is presented in Section 3.2.4.

3.1 XPS USING AL K α X-RAYS — ANALYSIS THROUGH THE ENTIRE DEPTH OF THE FILM

A preliminary XPS study of the interaction of O₂ with the Fe₈₄Cr₁₆ (001) surface was conducted. C and O were present on the unoxidized surface as noted in Section 2. The Fe and Cr 2p_{3/2} core-level peaks were deconvolved into one metallic and one oxidized peak each. Maschhoff and Armstrong showed that deconvolution of Fe 2p XPS spectra into Fe²⁺ and Fe³⁺ components is possible for Fe exposed to O₂ using electron energy loss spectra (EELS) and estimates for the relative heights and positions of satellite peaks.²⁶ We did not perform this additional deconvolution step due to the lack of EELS and satellite spectra for our sample. In addition, our films contained mixed Fe-Cr-O oxides (as discussed below), which would preclude constant positions for the Fe²⁺ and Fe³⁺ components. Representative Fe and Cr 2p core level spectra are shown in Figure 1.

The presence of carbon on the unoxidized surface controls the behavior of the relative Fe and Cr concentrations during initial oxygen exposures. In illustration, several atomic ratios, including deconvolved metal and oxide components, are shown in Figure 2. For the initial 1 L oxygen exposure, neither the iron-oxide nor chromium-oxide peak areas change appreciably. However, the measured Fe_{total}:Cr_{total} ratio increases by ~ 20% and the C concentration drops by a factor of ~ 4 (the C is virtually gone after the 5 L exposure, not shown in this figure). This behavior can be explained by the presence of a large concentration of carbidic C on the surface before oxygen exposure. This carbon is probably in the form of a two-dimensional "CrC" layer on the surface. [The segregation behavior of carbon on the Fe₈₄Cr₁₆ (001) surface has been discussed in detail in Ref. 18.] Some of the initial oxygen serves to oxidize the C on the surface, possibly resulting in CO formation, which is then desorbed into the vacuum. The surface reaction occurring may be similar to those for oxidation of bulk Cr₃C₂. Two examples are:



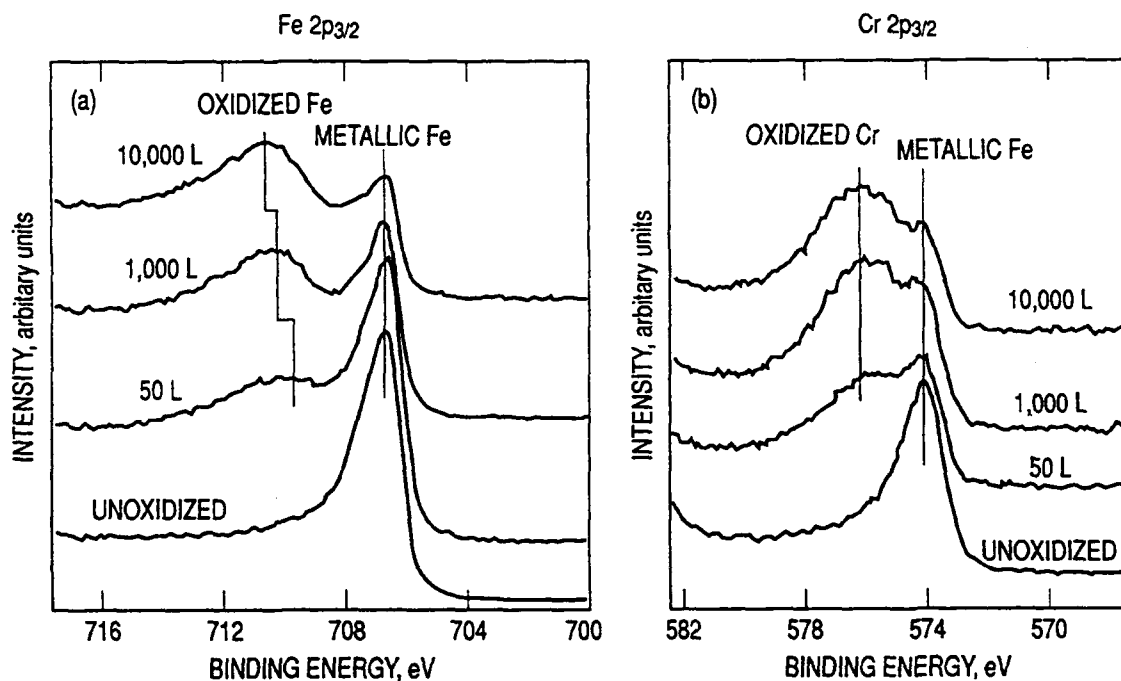


Figure 1. XPS spectra of the (a) Fe 2p_{3/2} and (b) Cr 2p_{3/2} core levels ($h\nu = 1486.6$ eV). Spectra are shown for the unoxidized surface and for surfaces exposed to 50 L, 1000 L, and 10,000 L of O₂. The positions of the oxide and metal components shown are derived by peak deconvolution. Binding energies are relative to the Au 4f_{7/2} peak at 83.9 eV.

Both of these bulk reactions are thermodynamically favorable (ΔG_{298}^0 values calculated from data in Ref. 13). Our data indicate little change in the Cr_{oxide} peak area for the first 1 L O₂ exposure. This is confirmed by the SXPS data (see Section 3.2.4). Therefore, the reaction occurring in the present study is probably similar to that shown in equation (2). The removal of the C from the "CrC" surface layer during initial oxidation apparently allows Fe to diffuse to the substrate surface, increasing the measured Fe_{total}:Cr_{total} ratio. The effect of segregated carbon on initial oxidation will be discussed further in Section 3.2.1.

For the 5 to 20 L O₂ exposure range, an appreciable amount of the Cr metal becomes oxidized, while Fe oxidizes at a slower rate. This is evident in Figure 2, curve (c), where the Fe_{oxide}:Cr_{oxide}

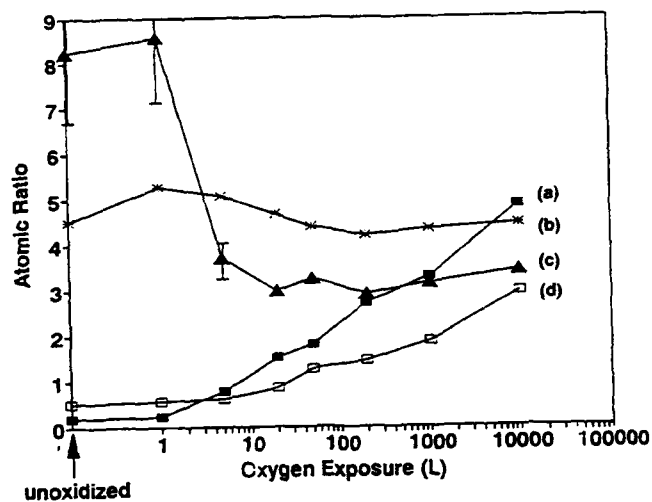


Figure 2. Variation of Fe:Cr and oxide:metal ratios as a function of oxygen exposure, determined by deconvolution of XPS Fe and Cr 2p core levels. Shown are (a) $\text{Cr}_{\text{oxide}}:\text{Cr}_{\text{metal}}$; (b) $\text{Fe}_{\text{total}}:\text{Cr}_{\text{total}}$; (c) $\text{Fe}_{\text{oxide}}:\text{Cr}_{\text{oxide}}$; (d) $\text{Fe}_{\text{oxide}}:\text{Fe}_{\text{metal}}$. Errors are estimated to be smaller than the symbol size except where noted with error bars.

ratio drops by a factor of 2 for 5 L and then drops another 20% for a 20 L exposure. As the overall amount of oxide increases during exposures to 200 L, the measured $\text{Fe}_{\text{oxide}}:\text{Cr}_{\text{oxide}}$ ratio [Figure 2, curve (c)] remains at a value that is less than the Fe:Cr ratio of the bulk alloy (i.e., ~ 3 vs 5.25). This causes the measured $\text{Fe}_{\text{total}}:\text{Cr}_{\text{total}}$ ratio to continue to decrease [Figure 2, curve (b)]. For O_2 exposures in the range 200 to 10,000 L, the $\text{Fe}_{\text{total}}:\text{Cr}_{\text{total}}$ ratio begins to rise slightly [Figure 2, curve (b)]. This rise is due to an increase in the $\text{Fe}_{\text{oxide}}:\text{Cr}_{\text{oxide}}$ ratio, but is also due to an increase in the $\text{Fe}_{\text{metal}}:\text{Cr}_{\text{metal}}$ ratio (not shown). Note that this rise is small here due to the relatively poor surface sensitivity of XPS (compared to SXPS). The $\text{Fe}_{\text{total}}:\text{Cr}_{\text{total}}$ ratio determined from SXPS changes faster because of greater surface sensitivity, as shown in Section 3.2.4.

The oxide thicknesses were determined from the formula $T = \lambda \cos \beta \cdot \ln(I_0/I)$, where T is the thickness of the film, λ is the inelastic mean free path of the electron, β is the angle between surface normal and the detection axis, I_0 is the intensity of the substrate peak for the unoxidized surface, and I is the intensity of the substrate peak after oxide film formation.²¹ These values were obtained for both the Fe and Cr $2p_{3/2}$ substrate peaks. The thickness obtained from the Cr $2p_{3/2}$ peak (22 Å) was higher than that for the Fe $2p_{3/2}$ core level (14 Å), primarily because of depletion of metal in the substrate near the metal/oxide interface, as discussed above. Therefore, the actual thickness value is probably closer to the value obtained for the Fe $2p_{3/2}$ peak since Fe is present in ~ 5 times the concentration in the substrate. Taking these considerations into account, and noting that the initial surface was not oxygen and carbon free, we have estimated an oxide film thickness of 16 ± 3 Å for the 10,000 L exposure.

Deconvolution of the Fe $2p_{3/2}$ and Cr $2p_{3/2}$ core levels revealed metallic components with the same binding energy (to within ± 0.05 eV) for all exposures. This indicates that the deconvolution procedure was adequate to unambiguously separate the oxide components from the metallic components. Binding energy differences between the oxide and metal components (Δ_{BE}) are plotted in Figure 3. The Δ_{BE} for the Cr $2p_{3/2}$ spectra is 2.1 ± 0.1 eV for all exposures, which is close to the average literature value of 2.4 ± 0.4 eV for Cr_2O_3 .²⁷⁻³¹ (The detected value may be lower because of screening effects, as discussed in Section 4.) The Δ_{BE} for the Fe $2p_{3/2}$ spectra, however, exhibits an increasing range of values, from ~ 2.0 eV at low exposures to 3.8 eV after the 10,000 L O_2 exposure. The 1 and 5 L values have a large uncertainty, but the value for 20 L O_2 (~ 2.3 eV) indicates predominantly Fe^{2+} , present either as FeO ($\Delta_{BE} = 2.7 \pm 0.3$ eV)³²⁻³⁵ or as FeCr_2O_4 ($\Delta_{BE} \sim 2.4$ eV).¹⁴ The value of 3.8 eV at 10,000 L is close to that for Fe_2O_3 ($\Delta_{BE} = 4.1 \pm 0.2$ eV),^{27,32-36} indicating that the film consists of predominantly Fe^{3+} at high exposures.

Changes in the widths of the oxide components of the Fe and Cr $2p_{3/2}$ core-level peaks with exposure level correspond to changes in the chemical homogeneity of the film and are shown in

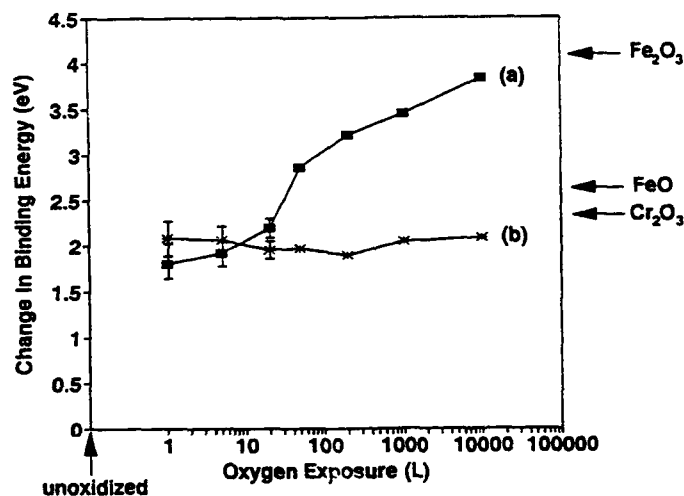


Figure 3. Difference in the binding energies of the oxide and metal contributions from XPS (i.e., Δ_{BE}), shown for (a) the Fe $2p_{3/2}$ peak and (b) the Cr $2p_{3/2}$ peak. Expected positions of the FeO and Fe_2O_3 peaks (i.e., for Fe $2p_{3/2}$), in addition to the Cr_2O_3 peak (i.e., for Cr $2p_{3/2}$) are shown on the right. Errors are estimated to be smaller than the symbol size, except where noted with error bars.

Figure 4. Neglecting the points with high uncertainty at 1 L O₂, clear trends are seen for each of the core levels. The Cr_{oxide} peak width is essentially constant, especially for exposures ≥ 20 L O₂ [Figure 4, curve (b)]. However, the Fe_{oxide} width rises in the range from 5 to 50 L, followed by a monotonic drop in width through the highest exposure [Figure 4, curve (a)].

These peak width changes, along with variations in peak areas and positions, are consistent with some initial conclusions. First, carbidic C present initially is removed in the early stages of O₂ exposure. The position and lack of variation of the Cr 2p_{3/2} oxide Δ_{BE} [Figure 3, curve (b)], along with the constant peak width [Figure 4, curve (b)], indicate that the Cr is in the form of Cr³⁺ throughout the film. On the other hand, the Fe 2p_{3/2} peak exhibits a wide variation in peak position and width. The peak positions in the early stages (~ 5 L O₂) are consistent with the presence of Fe, predominantly in the form of Fe²⁺. Continued O₂ exposure (20 to 50 L O₂) caused a sharp rise in BE [see Figure 3, curve (a)] and a concurrent rise in the width [Figure 4, curve (a)], indicating a mixture of Fe²⁺ and Fe³⁺. For larger exposures (200-10,000 L O₂), the drop in the width and continued increase in the BE of the Fe_{oxide} peaks indicate formation of an oxide layer that is predominantly Fe³⁺.

3.2 SOFT X-RAY PHOTOELECTRON SPECTROSCOPY (SXPS) - ANALYSIS OF THE SURFACE OF THE OXIDE FILM

3.2.1 SXPS Core Levels

The Fe and Cr 3p SXPS data are more representative of the chemical composition of the near-surface region than the Fe 2p_{3/2} and Cr 2p_{3/2} XPS data because lower photoelectron KEs were used (see Table 1). As discussed in Section 2, variations in the sample preparation procedures resulted in different Fe:Cr ratios at the surface of the unoxidized Fe₈₄Cr₁₆ alloy. In order to differentiate these surfaces, we introduce the quantity "R," which is defined as the atomic Fe:Cr

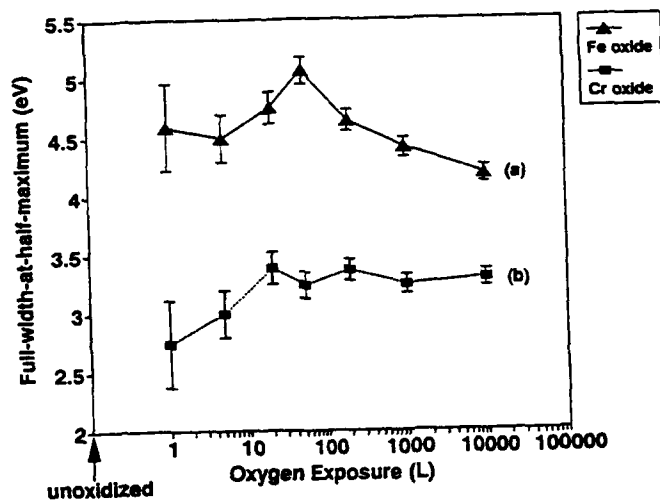


Figure 4. Full-widths-at-half-maximum (FWHM) for the deconvolved (a) Fe oxide and (b) Cr oxide XPS peaks (2p_{3/2} core levels).

ratio for the unoxidized surface determined from the Fe and Cr 3p core levels using $h\nu = 220$ eV. The R values for the three $\text{Fe}_{.84}\text{Cr}_{.16}$ (001) surfaces studied by SXPS were 10.5 for the 600°C anneal, 2.9 for the 775°C anneal, and 0.9 for the 800°C anneal. Previous studies of the surface segregation behavior of a $\text{Fe}_{.72}\text{Cr}_{.28}$ (011) crystal have shown that the clean, annealed surface is, in general, Cr-rich with respect to the bulk concentration.³⁷ However, in our study, the initial surface concentrations bracket the bulk ratio of 5.3, probably due to the lower Cr concentration in our sample. The observation that the surface concentration for the sample annealed to 600°C was Cr-poor compared to the bulk concentration may be due to a longer cool-down time for that sample or to the specific surface studied [(001) as opposed to (011)].

Because of the relatively extensive surface treatments for these samples, the surfaces were virtually oxygen-free (i.e., < 0.02 ML), and exhibited lower carbon contents than for the surface analyzed by XPS. The BEs (with respect to E_F) of the C 1s peaks for the unoxidized surfaces were all 282.5 ± 0.1 eV, which is close to that for Cr_3C_2 (282.8 eV³⁸), indicating that the C is initially carbidic, in agreement with Ref. 18. The quantities of carbon remaining on the surfaces were estimated using C 1s, Fe 3p, and Cr 3p peak areas from wide scans taken of the three surfaces using $h\nu = 600$ eV radiation (not shown here) and applying a procedure developed by Ebel³⁹ for the determination of thin-film thicknesses. The calculation assumes that the C is present as a thin film on top of the $\text{Fe}_{.84}\text{Cr}_{.16}$ (001) substrate. This assumption is justified by the rapid removal of C by low exposures of O_2 (as shown below and in Section 3.1), indicating that C is present only on the surface. Using this procedure, we calculated equivalent C thicknesses of 0.5, 0.7, and 0.5 (± 0.2) Å for the R = 0.9, 2.9, and 10.5 surfaces, respectively. Clearly, the large differences in R values do not correlate with C content at the surface. Rather, the differences in R values must be due to annealing conditions. Note, however, that the presence of C might influence the absolute R values, i.e., all the R values might have been higher had no C been present (this assumes that C forms into a "CrC" phase at the surface, as discussed in Ref. 18).

The Fe 3p and Cr 3p core levels for the unoxidized R = 2.9 surface, taken at both low KE ($h\nu = 130$ eV) and high KE ($h\nu = 220$ eV), are shown in Figure 5. After correcting for the small differences in relative photoelectron cross-sections, comparison of the Fe and Cr peak areas for the unoxidized surface in Figure 5, spectra (a) and (f) shows that there is a strong concentration gradient along the surface normal. Specifically, there is considerable segregation of Cr to the two topmost atomic layers of the surface; this surface exhibits Fe:Cr = 1.7 calculated from the $h\nu = 130$ eV spectrum, compared to R = 2.9 (i.e., calculated from the $h\nu = 220$ eV value). After the exposure of the surface to 10 L O_2 , the detected Cr was almost completely in the oxide form, as shown by the virtual disappearance of the metallic peak in favor of one that has shifted 2.2 eV to lower KE (higher BE) [Figure 5, spectrum (g)]. In contrast, the metallic Fe peak is still visible after the 10 L exposure, along with an oxide peak at 2.7 eV lower KE. Even after exposing the sample to 10,000 to 15,000 L O_2 , a metallic Fe contribution is still visible [Figure 5, spectra (c), (d), (h), and (i)] (confirmed by peak deconvolution; see Section 3.2.4). It is also clear that the Fe in the oxide layer has formed on top of the metallic Fe in the substrate. This can be seen by comparing spectrum (b) to spectrum (g) in Figure 5 for the 10 L exposure; the $\text{Fe}_{\text{oxide}}:\text{Fe}_{\text{metal}}$ ratio is greater for the low KE (i.e., more surface sensitive) spectrum.

As noted in Section 2, all three unoxidized surfaces exhibited sharp (001)-(1 x 1) LEED patterns with low backgrounds. During oxidation, the (1 x 1) spots became weaker, with a concurrent

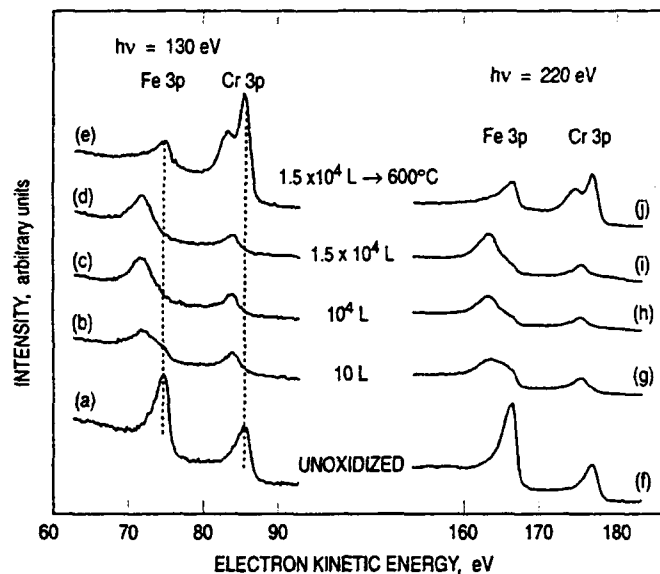


Figure 5. Fe 3p and Cr 3p core levels for the R=2.9 surface, taken both at low KE ($h\nu = 130$ eV) and high KE ($h\nu = 220$ eV), are shown for (a,f) the unoxidized surface, after (b,g) 10 L O_2 exposure, (c,h) 10,000 L O_2 exposure, (d,i) 15,000 L O_2 exposure, and (e,j) the 15,000 L surface subsequently heated to 600°C. Dotted lines show the positions of the metallic components in the low KE data.

increase in background intensity. For the highest O_2 exposures (10,000 to 15,000 L), the background was quite large, and the (1 x 1) pattern was only barely visible with a spot diameter ~ 3 times greater than that of the unoxidized surface. These results indicate the formation of an amorphous oxide film. This lack of long-range order may be due to shorter-range concentration gradients in the oxide film as well as lattice mismatch between the substrate and film. In addition, surface vacancy defects created during the oxidation of the thin C layer on the surface could have contributed to this lack of order.

In order to drive the state of the oxide film to thermodynamic equilibrium after the 15,000 L O_2 exposure, the R = 2.9 sample was heated to 600°C in UHV for 10 min [Figure 5, spectra (e) and (j)]. The anneal resulted in a virtual disappearance of the Fe-oxide component in favor of a metallic Fe component. In contrast, the relative amount of the Cr-oxide component increased, so that it is clearly greater than the Cr-oxide present in the oxide films for all exposures studied prior to annealing. Although the metallic Cr component also increased on annealing, the significant feature is that all oxygen remaining after the anneal is contained in a Cr-oxide phase. This results from the fact that Cr_2O_3 is more thermodynamically stable than any of the iron oxides¹³: when kinetic restraints are overcome by the increase in temperature, the iron oxides will decompose in favor of Cr_2O_3 . The behavior of $Fe_{.84}Cr_{.16}$ (001) surfaces heated after oxidation will be discussed in more detail in a subsequent publication⁴⁰.

Figure 6 shows core-level spectra for the $R = 10.5$ surface. More spectra were taken of this surface than the $R = 2.9$ and $R = 0.9$ surfaces to investigate the low- and intermediate-exposure regimes in greater detail. Comparison of the spectra for the unoxidized surface [Figure 6, spectra (a) and (l)] shows that although the near-surface concentration of Cr for this sample is lower than the nominal bulk value, there is a concentration gradient of Cr in the surface normal direction, as for the $R = 2.9$ sample. This sample shows behavior on oxidation that is similar to that for the $R = 2.9$ surface, with complete conversion of the Cr to the oxide state after the 10 L O_2 exposure [i.e., no detected metallic Cr; see Figure 6, spectrum (o)] and only partial oxidation of the Fe [i.e., persistence of the metallic Fe peak; see Figure 6, spectrum (d)]. Specific differences between the oxidation behavior of the two surfaces are discussed below.

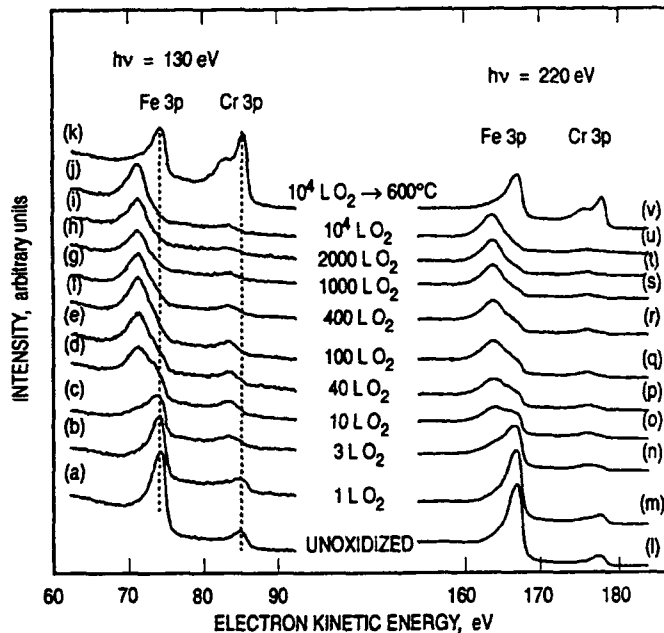


Figure 6. Fe 3p and Cr 3p core levels for the $R = 10.5$ surface, taken both at low KE ($h\nu = 130 \text{ eV}$) and high KE ($h\nu = 220 \text{ eV}$), are shown for (a,l) the unoxidized surface, after (b,m) 1 L O_2 exposure, (c,n) 3 L O_2 exposure, (d,o) 10 L O_2 exposure, (e,p) 40 L O_2 exposure, (f,q) 100 L O_2 exposure, (g,r) 400 L O_2 exposure, (h,s) 1000 L O_2 exposure, (i,t) 2000 L O_2 exposure, (j,u) $10,000 \text{ L O}_2$ exposure, and (k,v) the $10,000 \text{ L}$ surface subsequently heated to 600°C . Dotted lines show the positions of the metallic components in the low KE data.

Figure 7 shows representative results for deconvolution by least-squares fitting of the Fe 3p and Cr 3p core levels for the R = 10.5 surface. (The spectra for the R = 2.9 and R = 0.9 surface were also deconvolved; not shown.) These clearly show that the metallic Cr is virtually gone after the 10 L O₂ exposure [Figure 7, spectrum (h)], while the metallic Fe is detectable even after a 10,000 L exposure [Figure 7, spectrum (d)]. The deconvolved oxide and metal contributions will be used in Sections 3.2.2 and 3.2.4 to examine the variation of peak positions and concentration ratios with increasing O₂ exposure.

Spectra taken of the C 1s peak showed that the (carbide) C peak intensity dropped ~ 20% after exposing the sample to 1 L O₂ and dropped ~ 90% after the 3 L O₂ exposure. The 10 L O₂ resulted in the disappearance of the carbide peak. Note that oxygen exposure does not bury the carbide C beneath the oxide layer since XPS, which is less surface-sensitive, also showed a disappearance of C after exposure of the sample to 5 L O₂ (see Section 3.1). The O 1s peak area has virtually saturated after 10 L O₂. The position of the O 1s peak does not change during the experiment, in agreement with XPS results. This is not surprising since different transition metal oxides exhibit approximately the same O1s BE,²⁷ especially the various iron oxides.⁴¹

3.2.2 Energy Variation of SXPS Core Levels

The variation of Δ_{BE} values with O₂ exposure elucidates changes in the chemical state of the oxide film. The Δ_{BE} values for the Fe and Cr 3p spectra of the R = 10.5 surface are shown in Figure 8. Plots are shown for both the high KE [hv = 220 eV; curve (a)] and low KE [hv = 130 eV; curve (b)] spectra. The metallic Fe and Cr peak positions were the same to within ± 0.05 eV for all exposures, indicative of adequate deconvolution of the metallic and oxide components. The oxidized Fe peak position exhibited some variation, as shown in Figure 8, curves (a) and (b). The points for 1 L O₂ exposure are not shown because of their large uncertainty. Even the values for the 3 L O₂ exposure, on the curves for both Fe- and Cr-oxides, have relatively large errors associated with them, and so the significance of their position is tenuous. For the high KE Fe_{oxide} peak positions in the range 3 to 10,000 L O₂, the Δ_{BE} (between the oxide and metal contributions) varied ~ 0.5 eV (i.e., 2.6 to 3.1 eV). This range straddles the expected Δ_{BE} for Fe₂O₃ of 2.8 eV (± 0.15 eV),^{32,35,36,42} indicating that at the surface, increasing amounts of Fe in the form of Fe³⁺ are being produced (with a corresponding decrease in Fe²⁺) with increasing O₂ exposure. (Screening effects may affect the peak positions at low exposures; see Section 4). This is in general agreement with the XPS results (section 3.1), although different depths are being sampled. The observation of an Fe 3p Δ_{BE} that is greater than that for Fe₂O₃ supports the conclusion of a mixed Fe-Cr-O species in the oxide film, as discussed in Section 4.

The corresponding curves for the Cr 3p core level of the R = 10.5 surface [Figure 8, curves (c) and (d)] show that the high KE Cr-oxide peak position varies less than for the Fe-oxide peak position. This is consistent with the XPS data that indicated that Cr was essentially in one oxidation state (i.e., Cr³⁺) for all exposures. However, there is a small increase in Δ_{BE} with increasing O₂ exposure, from ~ 1.6 eV in the 3 to 100 L range to ~ 1.9 eV at 10,000 L [Figure 8, curve (c)]. The initial value is close to that for Cr₂O₃, 1.5 \pm 0.1 eV.^{29,30} Except at the highest exposures, the low KE Cr_{oxide} curve [Figure 8, curve (d)] follows the curve for the high KE curve.

The R = 2.9 and R = 0.9 surfaces exhibit Fe and Cr 3p Δ_{BE} curves (not shown) that show trends similar to those for the R = 10.5 surface discussed above. Although a detailed comparison is precluded by the relative scarcity of data points for the R = 2.9 and R = 0.9 surfaces, their Δ_{BE}

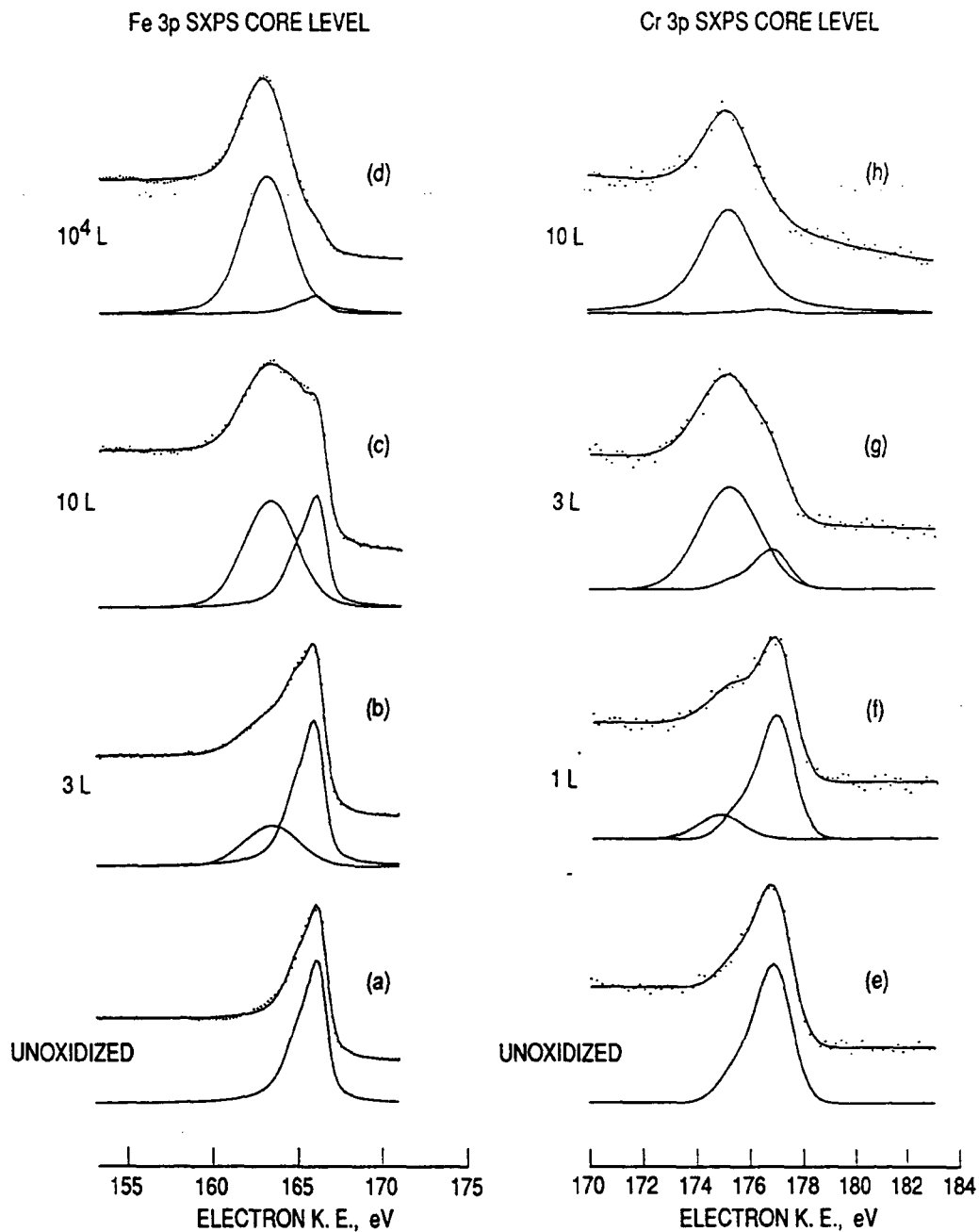


Figure 7. Results of deconvolution by least-squares fitting of the high KE ($h\nu = 220$ eV) Fe 3p and Cr 3p core-level spectra to a combination of an oxide and a metallic peak. Results for the Fe 3p core level are shown for (a) a unoxidized surface, (b) 3 L O_2 , (c) 10 L O_2 , and (d) 10,000 L O_2 . Results for the Cr 3p core level are shown for (e) a unoxidized surface, (f) 1 L O_2 , (g) 3 L O_2 , and (h) 10 L O_2 . For each spectrum, the results of the fit (line) are overlaid on the raw data (dots). Below these are the oxidized and metallic contributions.

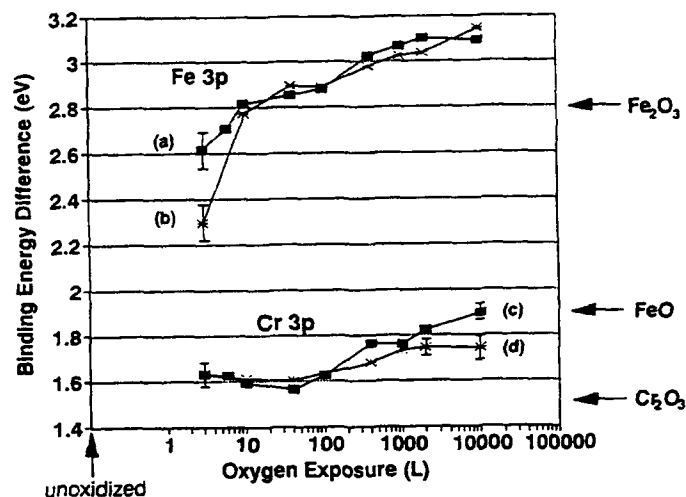


Figure 8. Difference in the oxide and metal 3p peak BEs (denoted Δ_{BE} in text) determined by deconvolution of the SXPS core levels taken of the $R=10.5$ surface. For the Fe 3p core level, data for (a) the high KE ($h\nu = 220$ eV) and (b) low KE ($h\nu = 130$ eV) spectra are shown. For the Cr 3p core level, data for (c) the high KE ($h\nu = 220$ eV) and (d) low KE ($h\nu = 130$ eV) spectra are shown. Expected positions for Fe-oxides and Cr_2O_3 are shown on the right side of the figure. An increase in Δ_{BE} corresponds to an increase in the oxide BE. Errors are estimated to be smaller than the symbol size, except where noted with error bars.

values are close (± 0.1 eV) to those of the $R = 10.5$ surface at corresponding O_2 exposures. Therefore, similar species are present during oxidation of $Fe_{.84}Cr_{.16}$ (001) surfaces with different initial Cr concentrations. As will be discussed in Section 3.2.4, the main difference in the oxidation behavior of these surfaces is the relative amounts of these species.

3.2.3 SXPS Valence Band Spectra

Valence band spectra are also sensitive to the chemical state in the oxide film. These are shown for the $R = 10.5$ surface in Figure 9, taken at photon energies of 154 and 254 eV. The shapes of the spectra for the unoxidized surface [Figure 9, spectra (a) and (k)] are consistent with that for a clean metallic surface.⁴¹ For the oxidized surfaces, the main difference between the spectra taken for different photon energies is that of depth sensitivity since the Fe 3d cross-section only increases slightly relative to the O 2p cross-section between 154 and 254 eV.²⁵ With initial oxygen exposure (1 to 3 L O_2), two shoulders appear at ~ 3 and ~ 6.5 eV BE [Figure 9, spectra (b), (c), (l), (m)]. Increasing O_2 exposure results in increasing intensity in a large envelope centered at ~ 5 eV and reduction of the metallic 3d peak near E_F [Figure 9, spectra (d)-(i) and (n)-(s)].

The $h\nu = 154$ eV valence bands for the middle- and high-exposure regions (10 to 10,000L) are similar to valence band spectra taken for Fe_2O_3 (i.e., Fe^{3+}), coexisting with some remaining Fe-metal. However, the spectra also exhibit some similarities to those for Fe_3O_4 and FeO (i.e., some amount of Fe^{2+}); the broad valence band envelopes are typical of iron oxides in general.^{32,41} For higher exposures (1000 to 10,000 L), Figure 9, spectra (h) and (i) display a weak satellite at

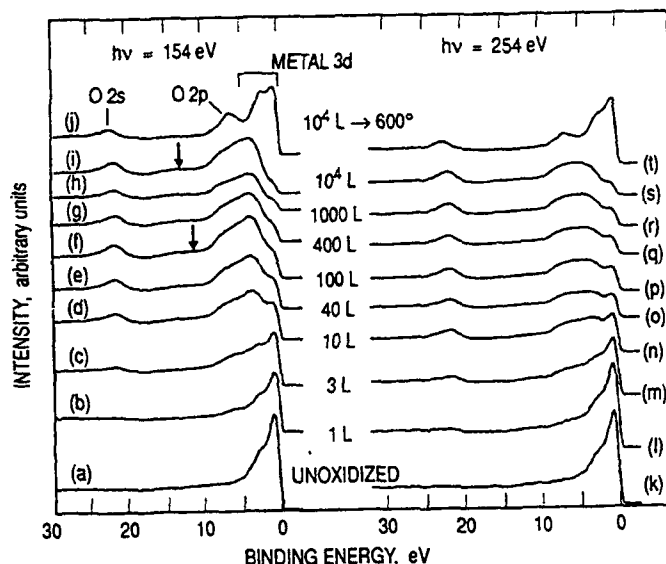


Figure 9. Valence band spectra of the $R = 10.5$ surface taken with $h\nu = 154$ and 254 eV. Spectra are shown for (a,k) the unoxidized surface, after (b,l) 1 L O_2 exposure, (c,m) 3 L O_2 exposure, (d,n) 10 L O_2 exposure, (e,o) 40 L O_2 exposure, (f,p) 100 L O_2 exposure, (g,q) 400 L O_2 exposure, (h,r) 1000 L O_2 exposure, (i,s) 10,000 L O_2 exposure, and (j,t) the 10,000 L surface subsequently heated to 600°C . Spectra are referenced to E_F .

~ 14 eV, indicating the presence of predominantly Fe^{3+} . A surface that is predominantly Fe^{2+} would be expected to display a satellite at 10 to 11 eV.⁴¹ In fact, the large width of this satellite region between 10 and 15 eV BE at medium exposures (i.e., 10 to 100 L O_2) is consistent with the presence of a mixture of Fe^{2+} and Fe^{3+} .

When the surface that had been exposed to 10,000 L O_2 was heated to 600°C , reducing the iron and leaving a chromium oxide (see Figures 5 and 6), the valence band spectrum consisted of a metallic 3d peak, a Cr-oxide 3d peak, and a Cr-oxide O 2p peak [Figure 9, spectra (j) and (t)]. This well-defined structure is typical of Cr_2O_3 , which exhibits better separation of the O 2p and Cr 3d peaks than oxides of iron and other metals.⁴³ Comparison of these spectra to those for the 1 L exposure [Figure 9, spectra (b) and (l)] and the 3 L exposure [Figure 9, spectra (c) and (m)] confirms that much of the metallic species present in the initial oxide film consists of Cr in the 3+ state.

3.2.4 Variation of Surface Concentrations During O_2 Exposure: Comparison of Different Initial Surfaces

Comparison of the oxide:metal ratios for films on surfaces with different R values gives a qualitative description of trends in the oxide film thickness. The variations in the $Cr_{\text{oxide}}:Cr_{\text{metal}}$ ratio for the three different surfaces are shown in Figure 10. The disappearance of the Cr-metal con-

tribution after the 10 L O₂ exposure, discussed in Section 3.2.1, is demonstrated by a Cr_{oxide}:Cr_{metal} ratio that is > 30 for the R = 10.5 and 2.9 surfaces for O₂ exposures ≥ 10 L [Figure 10, curves (a) and (b)]. This is in contrast to the Cr_{oxide}:Cr_{metal} ratio determined from XPS [Figure 2, curve (c)], which shows that the lower surface sensitivity of XPS allows detection of the metallic Cr under the oxide layer.

The corresponding Fe_{oxide}:Fe_{metal} ratios are shown in Figure 11. In all cases, the ratio rises but does not approach infinity as does the Cr_{oxide}:Cr_{metal} ratio, even for the highest exposures. At low exposures, the R = 2.9 surface [Figure 11, curve (b)] exhibits a higher Fe_{oxide}:Fe_{metal} ratio than for the R = 10.5 surface [Figure 11, curve (a)], but for higher exposures, just the opposite occurs. This indicates that the "stainless" property of high-Cr steels may be operative for highly oxidative environments (e.g., exposure to atmosphere) where enough oxygen is present to form a complete, passivating Cr-rich layer. The reason that the Fe_{oxide}:Fe_{metal} ratio for the R = 2.9 surface is actually *higher* than for R = 10.5 surface at 10 L exposure is simply that there is a lower concentration of Fe near the surface available to be oxidized. The *total* Fe_{oxide} fraction is actually the same; i.e., the Fe_{oxide}/(Fe_{oxide} + Fe_{metal} + Cr_{oxide} + Cr_{metal}) ratio is 0.5 (within ± 0.02) for both the R = 10.5 and 2.9 surfaces.

In contrast with the other two surfaces, the R = 0.9 surface exhibits the lowest Fe_{oxide}:Fe_{metal} ratio for *all* exposures studied [Figure 11, curve (c)], indicating formation of a thinner oxide film. In addition, the metallic Cr peak for the R = 0.9 surface remains detectable for an O₂ exposure as high as 100L [Figure 10, curve (c)]. These observations are consistent with the idea that the unoxidized R = 10.5 and 2.9 surfaces have a non-negligible concentration of Fe in the top monolayer, while the unoxidized R = 0.9 surface may have a virtually complete Cr monolayer at

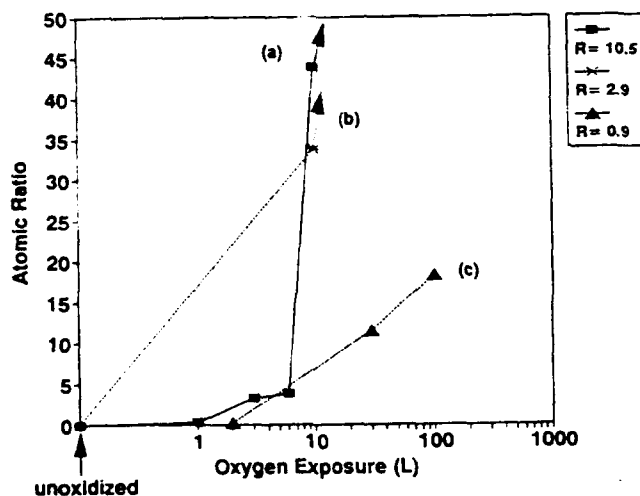


Figure 10. Cr_{oxide}:Cr_{metal} ratios for the three surfaces studied by SXPS. Shown are ratios for (a) the R = 10.5 surface, (b) the R = 2.9 surface, and (c) the R = 0.9 surface. High KE core levels were used (i.e., hv = 220 eV).

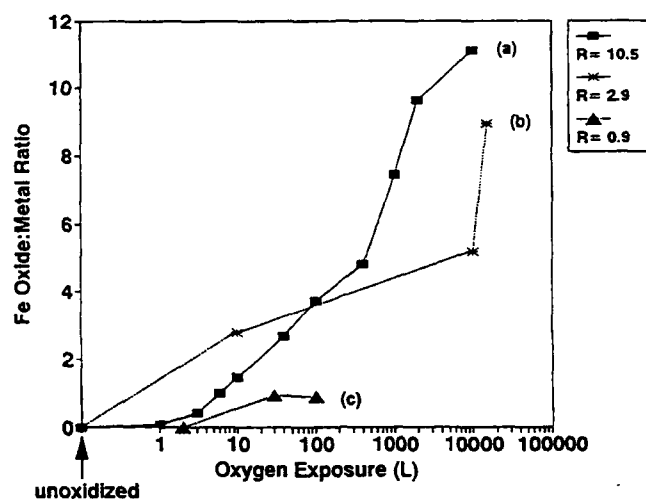


Figure 11. $\text{Fe}_{\text{oxide}}:\text{Fe}_{\text{metal}}$ ratios for the three surfaces studied by SXPS. Shown are ratios for (a) the $R = 10.5$ surface, (b) the $R = 2.9$ surface, and (c) the $R = 0.9$ surface. High KE core levels were used (i.e., $h\nu = 220$ eV).

the surface. Therefore, the $R = 0.9$ surface can form a Cr-rich passivating layer at the lowest O_2 exposures, while the other two surfaces have no initial barrier to diffusion of Fe.

To confirm that the oxide film grows on top of the metallic substrate and to determine the abruptness of the oxide/metal interface, a qualitative "depth distribution" of surface components can be constructed. This was done by comparing the Fe 3p core-level spectra taken at the two different photon energies used in this study. Graphically, this is presented as the $\text{Fe}_{\text{oxide}}:\text{Fe}_{\text{metal}}$ ratio determined at high KE ($h\nu = 220$ eV) divided by the same ratio determined at low KE ($h\nu = 130$ eV). A value of this quantity that is < 1 would indicate enhancement of oxidized Fe (compared to metallic Fe) in the top 1 to 2 ML of the surface compared to the top 3 to 4 ML. Figure 12(a) presents such a graph for the high and low KE $\text{Fe}_{\text{oxide}}:\text{Fe}_{\text{metal}}$ ratios for all three surfaces. As expected, the values are consistently < 1 , indicating growth of the oxide film on top of the metallic substrate.

The significance of the shape of Figure 12(a) can be better understood by comparing it to a simulated curve for a model system, i.e., an abrupt interface. Figure 12(b) shows the results of a calculation performed to simulate the ratio plotted in Figure 12(a), except that it is plotted versus oxide film thickness rather than the logarithm of the oxygen exposure. The algorithm used for calculating the curve in Figure 12(b) was derived from formulas developed by Ebel for analysis of SiO_2 films on Si,³⁹ but we used IMFP values from Table 1. This calculation assumes an oxide film of uniform thickness and an abrupt metal/oxide interface (significant mixing across the interface would give a slope ≥ 0). The general downward trend is similar in Figures 12(a) and (b), although the shapes would be expected to be different since the oxide thickness is not necessarily proportional to the logarithm of the oxygen exposure. However, the initial values are close

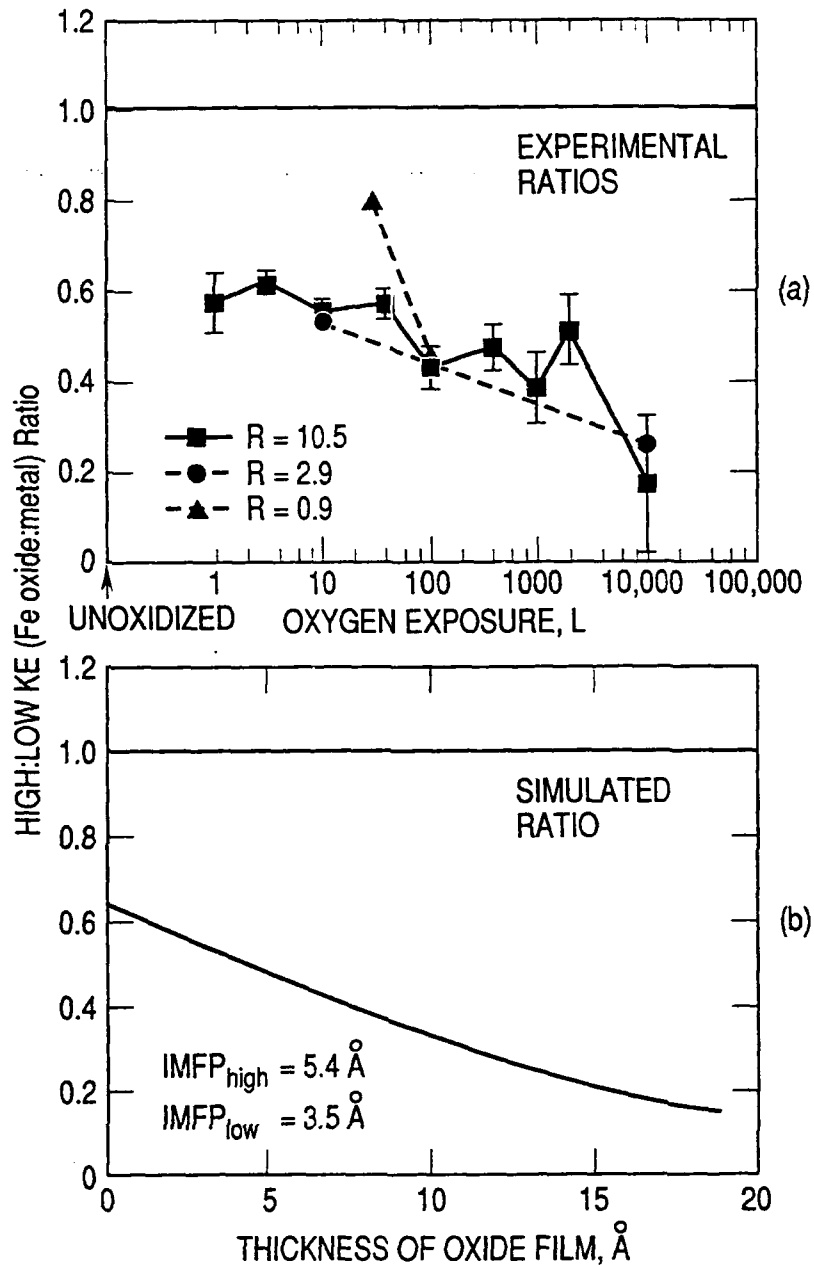


Figure 12. The high KE $Fe_{oxide}:Fe_{metal}$ ratios divided by the same ratio determined from low KE data (see text). A value of <1 implies enhancement of oxidized Fe over metallic Fe at the surface compared to deeper layers. The curves in (a) were experimentally determined and plotted versus O_2 exposure, while the curve in (b) was determined using formulas in Ref. 39 and plotted versus oxide film thickness. Estimated errors shown as bars on the curve for the $R = 10.5$ surface are typical for points at comparable exposures on the curves for the $R = 2.9$ and $R = 0.9$ surfaces.

(i.e., ~ 0.6), and the 10,000 L value in Figure 12(a) (i.e., ~ 0.2) is close to that for the 16 Å value in Figure 12(b). (Note that in Section 3.1, the thickness of the oxide film after a 10,000 L O₂ exposure was estimated by XPS to be 16 ± 3 Å; a similar value, 17 Å, was obtained for the oxide thickness of the R = 10.5 surface at 10,000 L exposure). The similarity between Figures 12(a) and (b) (both curves approach zero for large O₂ exposure) is consistent with an abrupt oxide/metal interface and uniform film growth.

Previous studies (especially those using AES) have discussed the changes in the surface region of Fe-Cr alloys during O₂ exposure in terms of variation of the Fe_{total} and Cr_{total} quantities rather than the individual oxide and metal components. For comparison, we present a graph of the Fe_{total}:Cr_{total} ratio determined from the hv = 220 eV core-level data in Figure 13. The enhanced surface sensitivity of SXPS is shown by comparison of the Fe_{total}:Cr_{total} ratios in Figure 13 to those analyzed by XPS [Figure 2, curve (b)]. The SXPS curves exhibit more relative movement than that determined by XPS. The prominent features of Figure 13, curve (a), for the R = 10.5 surface, are a drop in the ratio with initial O₂ exposure, a plateau at 10 to 100 L, and a subsequent rise in the ratio in the range 400 to 10,000 L O₂. The other two surfaces are consistent with this behavior. The same plots for the low KE data (hv = 130 eV, not shown here) show similar behavior to the high KE data, but exhibit some differences in shape. The cause of these differences is discussed below.

The various regimes of growth as a function of O₂ exposure shown in Figure 13 can be better understood by examining the relative concentrations of the oxides with increasing oxygen exposure. The Fe_{oxide}:Cr_{oxide} ratios for the three surfaces studied are shown in Figure 14. The low initial values of these curves confirm that the initial oxide films are richer in Cr than the unoxidized surfaces. For the R = 10.5 surface, increasing exposures of O₂ result in a steady increase in the Fe_{oxide}:Cr_{oxide} ratio, until for the highest exposure (10,000 L), the Cr concentration in the oxide film is actually lower than that for the unoxidized surface [Figure 14, curve (a)].

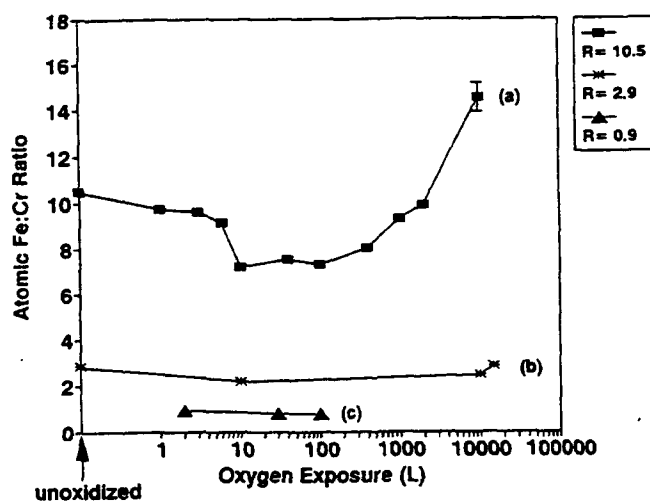


Figure 13. Fe_{total}:Cr_{total} [(Fe_{oxide}+Fe_{metal})/(Cr_{oxide}+Cr_{metal})] ratios for (a) the R = 10.5 surface, (b) the R = 2.9 surface, and (c) the R = 0.9 surface. High KE core levels were used (i.e., hv = 220 eV). Errors are estimated to be smaller than the symbol size, except where noted with error bar.

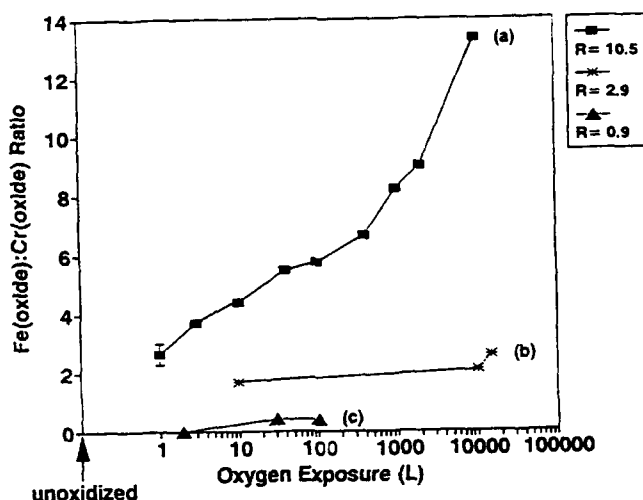


Figure 14. $\text{Fe}_{\text{oxide}}:\text{Cr}_{\text{oxide}}$ ratios for (a) the $R = 10.5$ surface, (b) the $R = 2.9$ surface, and (c) the 0.9 surface. High KE core levels were used (i.e., $h\nu = 220$ eV). Errors are estimated to be smaller than the symbol size, except where noted with error bar.

Therefore, the initial drop in the measured $\text{Fe}_{\text{total}}:\text{Cr}_{\text{total}}$ ratio [Figure 13, curve (a)] is caused by the formation of a relatively Cr-rich oxide film. The plateau and subsequent rise in Figure 13, curve (a) are caused by the increasing $\text{Fe}_{\text{oxide}}:\text{Cr}_{\text{oxide}}$ ratio (Figure 14), along with the persistence of the Fe_{metal} 3p peak after the Cr_{metal} 3p peak has disappeared.

Comparison of the three surfaces in Figure 14 shows clearly that the excess Cr at the surface suppresses the oxidation of Fe at higher exposures by forming a Cr-enriched oxide film that acts as a diffusion barrier. For example, comparison of curves (a) and (b) at 10,000 L O_2 exposure shows that the low-Cr $R = 10.5$ surface possesses an oxide film that is enriched in Fe with respect to the unoxidized surface (i.e., $\text{Fe}_{\text{oxide}}:\text{Cr}_{\text{oxide}} = 13.3$), while the oxide film on the $R = 2.9$ surface is depleted in Fe with respect to the unoxidized surface (i.e., $\text{Fe}_{\text{oxide}}:\text{Cr}_{\text{oxide}} = 2.1$). Even the 15,000 L exposure for the $R = 2.9$ surface exhibits a value ($\text{Fe}_{\text{oxide}}:\text{Cr}_{\text{oxide}} = 2.6$) that is lower than that for the unoxidized surface.

In order to evaluate the relative depth distribution of Fe and Cr within the oxide film, the high KE $\text{Fe}_{\text{oxide}}:\text{Cr}_{\text{oxide}}$ ratio was divided by the ratio for low KE; the result is shown in Figure 15 (presented similarly to Figure 12 for the $\text{Fe}_{\text{oxide}}:\text{Fe}_{\text{metal}}$ ratios). The plot for the $R = 10.5$ surface shows a ratio that is >1 at low exposures (1 to 30 L), indicating that the oxidized Cr species is, on the average, actually closer to the surface of the film than the oxidized Fe species. This is probably due to a combination of the initial surface enhancement of Cr and the greater thermodynamic driving force to produce Cr-containing oxides rather than Fe-oxides. As the exposure level is increased (100 to 10,000 L O_2), the curve for the $R = 10.5$ surface exhibits values <1 , indicating that Fe has preferentially segregated to the surface of the oxide film. However, the $R = 10.5$ curve increases from 1000 to 10,000 L O_2 exposure. This increase indicates that some Cr is

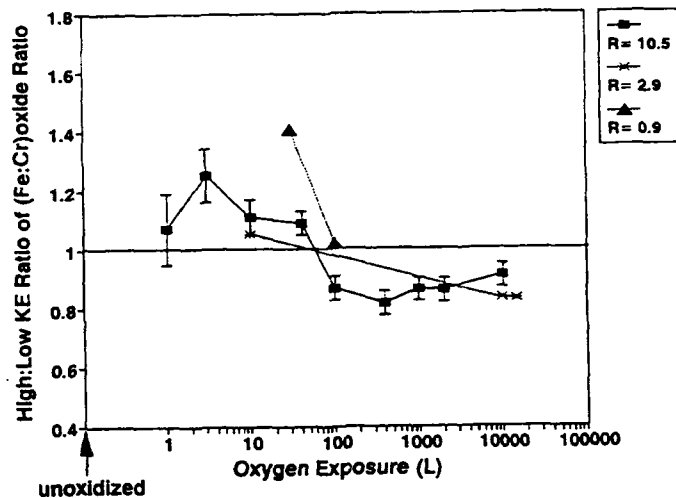


Figure 15. The high KE $\text{Fe}_{\text{oxide}}:\text{Cr}_{\text{oxide}}$ ratio divided by the same ratio determined from low KE data (see text). A value of <1 implies enhancement of oxidized Fe over oxidized Cr at the surface compared to deeper layers. Estimated errors shown as bars on the curve for the $R = 10.5$ surface are typical for points at comparable exposures on the curves for the other two surfaces.

still present near the surface of the growing oxide film at high exposures. The increase in slope, indicating mixing of Cr and Fe in the oxide film, contrasts with the consistently negative slope in Figure 12(a) of the high KE $\text{Fe}_{\text{oxide}}:\text{Fe}_{\text{metal}}$ ratio divided by that for the low KE ratio. That plot indicated no mixing between the Fe-metal and the Fe-containing oxide film.

The high:low KE $\text{Fe}_{\text{oxide}}:\text{Cr}_{\text{oxide}}$ plots for the $R = 2.9$ and 0.9 surfaces (Figure 15) are qualitatively similar to that for the $R = 10.5$ surface in that they both decrease with increasing O_2 exposure. In addition, the $R = 2.9$ plot also shows the transition from >1 to <1 as the relatively Cr-rich oxide film is covered by the Fe-rich oxide film. Note that although the $\text{Fe}_{\text{oxide}}:\text{Cr}_{\text{oxide}}$ ratios are quite different in magnitude between the three surfaces (see Figure 14), the depth distributions may not be that different (compare curves for the $R = 10.5$ and 2.9 surfaces in Figure 15). This indicates that the same phases may be present near the surface of the oxide films, although the relative concentrations within the Cr-containing phases may be somewhat different between samples with different R values.

4. DISCUSSION

The results of this study reveal some general conclusions about the mechanism of oxide film growth in Fe-Cr alloys. The formation of a Cr-enhanced oxide for low exposures is supported by the greater thermodynamic stability of Cr-containing oxides such as Cr_2O_3 (and mixed oxides like FeCr_2O_4) versus the iron oxides FeO , Fe_3O_4 , and Fe_2O_3 .¹³ In addition, since Cr tends to segregate on the unoxidized surface, oxygen should react predominantly with Cr for low exposures. The rate of oxidation drops quickly with increasing exposure as a "passivating" Cr-enhanced oxide layer is formed. At exposures of 30 to 100 L O_2 , a region of diffusion-controlled growth is entered as the oxide layer becomes increasingly Fe-rich. This "thermodynamic-to-kinetic transition" occurs because the relative mobility of Fe in solids is considerably higher than for Cr.¹⁴⁻¹⁶ Therefore, the Fe atoms have a greater probability of diffusing through the film to be oxidized than do the Cr atoms. For exposures of O_2 near atmospheric exposure (i.e., ~ 5 orders of magnitude greater than the highest exposure in the present study), a further decrease and eventual disappearance of Cr-containing species in the top few Ångstroms at the surface should result, as discussed below.

Comparison between the Δ_{BE} core-level results for the XPS and SXPS can elucidate the depth distribution of species in the growing oxide film even though the relative concentrations of the compounds present on the surfaces analyzed by the two techniques may be different. The specimen studied by XPS was annealed to ~ 700°C, which is in the middle of the anneal temperatures of 600°C, 775°C, and 800°C for the surfaces studied by SXPS. (The cool-down rate was somewhat slower for the sample that was prepared for XPS analysis, which affects the surface composition in an undetermined manner.) XPS is consistent with the formation of oxidized Fe, predominantly in the form of Fe^{2+} at low O_2 exposures, followed by a mixed film ($\text{Fe}^{2+}/\text{Fe}^{3+}$) at intermediate exposures and predominantly Fe^{3+} at high exposures. Comparison of the SXPS and XPS results indicates that the Fe at the surface of the oxide film has a higher fraction of Fe^{3+} than the rest of the film throughout the range of exposures [compare Figure 3, curve (a) to Figure 8, curves (a) and (b)]. The energy of the oxide component of the Cr 3p core level from SXPS appears to vary more than that for the Cr 2p_{3/2} core level from XPS [compare Figure 3, curve (b) to Figure 8, curves (c) and (d)]. This indicates that the species present at the surface change with increasing O_2 exposure. In contrast, the relatively Cr-rich region of the oxide film near the metal/oxide interface (as measured by XPS) remains in essentially the same chemical state throughout the oxidation process.

The SXPS results clearly show that exposure of the $\text{Fe}_{.84}\text{Cr}_{.16}$ (001) surface to $\leq 10,000$ L O_2 results in a mixed Fe-Cr-O film rather than a bilayer structure with a pure Fe_2O_3 on top of a Cr_2O_3 or FeCr_2O_4 layer. This is shown by the persistence of the Cr 3p peak at the higher exposures (10,000 to 15,000 L O_2) taken under surface-sensitive conditions [i.e., see Figure 5, spectrum (d) and Figure 6, spectrum (j)]. In addition, comparison of the oxide components of the Fe and Cr 3p core levels taken for two different photoelectron KEs shows that the oxide film cannot be described as a pure Fe-oxide layer on top of a pure Cr-oxide layer with a sharp, well-delineated interface (see discussion of Figure 15 in Section 3.2.4). Rather, the film exhibits an apparently smooth concentration gradient, with increasing amounts of Fe toward the surface of the film.

It was shown in Section 3.2.2 that higher exposures (i.e., 400 to 10,000 L O₂) result in Fe and Cr 3p SXPS Δ_{BE} values that are both higher than that for Fe₂O₃ and Cr₂O₃, respectively (see Figure 8). Although the existence of a separate, pure Fe₃O₄ phase cannot be ruled out, it is unlikely since the BE of the Fe³⁺ component of the Fe 3p core level of Fe₃O₄ should be the same⁴¹ or lower^{32,35,44} than that for Fe₂O₃. (Only one available study⁴² shows a higher BE for Fe₃O₄.) Referencing problems can be ruled out as a cause of these high Δ_{BE} values because of the invariance of the metallic Fe 3p and O 1s peak positions after all oxygen exposures (see Sections 2 and 3.2.1, respectively). However, it is necessary to examine the possibility of screening of the oxide core levels by valence electrons in the metallic, conducting substrate. Screening could cause the unusually low Δ_{BE} values for the 1 and 3 L exposures because of the thinness of the film (see for example Ref. 45). A decrease in screening as the film thickness is increased might be partly the cause of the subsequent rise at higher exposure levels. However, correcting the Δ_{BE} values for screening would result in *even higher* Δ_{BE} values for the highest exposures, so screening is not the cause of the unexpectedly high Δ_{BE} values seen in Figure 8.

The anomalously high Δ_{BE} values could indicate the formation of an amorphous phase similar to the spinel Fe_{1+x}Cr_{2-x}O₄ since the only compounds that have higher 3p BEs (and therefore higher Δ_{BE} 's) than the sesquioxides and contain Fe, Cr, and/or O are these mixed oxide spinels.^{14,46} Specifically, the BE of Fe_{1+x}Cr_{2-x}O₄ with x ≥ 1.0 was shown in Ref. 14 to be greater than that of Fe₂O₃ (see Table 2). In addition, the Cr 3p BE for Fe_{1+x}Cr_{2-x}O₄ with x ≥ 0.4 is greater than that for Cr₂O₃.¹⁴ This interpretation is also consistent with the XPS results in that the range of Fe 2p_{3/2} Δ_{BE} values for Fe_{1+x}Cr_{2-x}O₄ with 0 ≤ x ≤ 1.4 mostly fall between those for FeO and Fe₂O₃. In addition, the Cr 2p_{3/2} Δ_{BE} value for Cr₂O₃ is the same as that for FeCr₂O₄ (see Table 2). Note that the mixed oxide Fe_{1+x}Cr_{2-x}O₄ contains both Fe²⁺ and Fe³⁺ for x > 0. It was shown in Ref. 14 that this results in an increase in the Fe photoelectron peak widths compared to Fe₂O₃. It is curious that these mixed oxides exhibit Fe 2p_{3/2} BEs that are lower than that for Fe₂O₃ while they exhibit Fe 3p BEs that are higher (for x ≥ 1.0) than that for Fe₂O₃. This discrepancy, which is probably based on final state effects, was not explained in Ref. 14, nor will such an explanation be attempted here. Our intention is simply to use their BE values to support the presence of a Fe_{1+x}Cr_{2-x}O₄-like species in the oxide film in the present study.

Table 2. Binding Energies of Fe_{1+x}Cr_{2-x}O₄ Spinels (Taken From Ref. 14)

Compound	Binding Energy (eV)			
	Fe		Cr	
	2p _{3/2}	3p	2p _{3/2}	3p
Fe ₂ O ₃	711.2	55.8	-	-
Fe _{2.4} Cr _{0.6} O ₄	710.8	56.4	576.8	44.5
Fe _{2.0} Cr _{1.0} O ₄	710.9	56.1	576.6	44.2
Fe _{1.4} Cr _{1.6} O ₄	710.4	55.8	576.4	44.1
Fe _{1.0} Cr _{2.0} O ₄	709.5	55.0	576.2	43.7
α-Cr ₂ O ₃	-	-	576.3	43.7

The presence of the mixed oxide, i.e., an $\text{Fe}_{1+x}\text{Cr}_{2-x}\text{O}_4$ -like species, in the oxide film is supported by a previous XPS sputter-depth-profiling study of Fe-Cr alloys with 6-20% Cr that were oxidized at room temperature⁹ and by an XPS/SIMS study that included data on a 304 stainless-steel surface exposed to atmosphere at room temperature.¹⁵ In addition, a number of studies have provided evidence of $\text{Fe}_{1+x}\text{Cr}_{2-x}\text{O}_4$ formation on the surface of Fe-Cr alloys and Cr-containing steels that were heated to temperatures of 200°C to 600°C during oxidation and studied by AES,^{3-5,10} XPS,^{5,15} LEED,¹⁰ RHEED,⁷ Raman,⁸ SIMS,¹⁵ and Mössbauer spectroscopy.⁶ The results of Young and Mitchell indicated that spinel formation might be more likely for lower oxidation temperatures and oxygen exposures.⁷

The formation of a $\text{Fe}_{1+x}\text{Cr}_{2-x}\text{O}_4$ -like species is also supported on thermodynamic grounds. For example, the reaction $\text{FeO} + \text{Cr}_2\text{O}_3 \rightarrow \text{FeCr}_2\text{O}_4$ is exothermic, with $\Delta G_{298}^\circ = -19$ kcal/mole.¹³ Therefore, the fact that the metal atoms in the films are predominantly in the form of Fe^{2+} and Cr^{3+} at low exposures (≤ 10 L O_2) is consistent with the presence of FeCr_2O_4 (with a possible small excess of FeO) rather than Cr_2O_3 and relatively large amounts of FeO. For higher exposures, both Fe^{2+} and Fe^{3+} are present in addition to Cr^{3+} , so the binary compound Fe_3O_4 (which has a $\text{Fe}^{3+}:\text{Fe}^{2+}$ ratio of 2) might be expected. However, any addition of Cr to Fe_3O_4 to form $\text{Fe}_{1+x}\text{Cr}_{2-x}\text{O}_4$ results in a free energy decrease, favoring the ternary mixed oxide.⁴⁷ Although the presence of Fe_3O_4 cannot be ruled out, it is likely that as long as any Cr and Fe^{2+} remain in the oxide film, then an $\text{Fe}_{1+x}\text{Cr}_{2-x}\text{O}_4$ -like species will be formed. Any excess Fe^{3+} would exist as Fe_2O_3 , as for the higher O_2 exposures. This is demonstrated by deconvolution of the Fe 3p peak for the 10,000 L exposure on the $R = 10.5$ surface, which showed that the $\Delta_{\text{BE}} = 3.1$ value was consistent with a mixture of $\text{Fe}_{2.4}\text{Cr}_{.6}\text{O}_4$ and Fe_2O_3 [Figure 8, curves (a) and (b)]. The presence of $\text{Fe}_{1+x}\text{Cr}_{2-x}\text{O}_4$ with values of $x > 1.4$ (and correspondingly smaller amounts of Fe_2O_3) would also be consistent. As a result, exact determination of x in the $\text{Fe}_{1+x}\text{Cr}_{2-x}\text{O}_4$ phases, along with their concentrations in the film, is beyond the scope of this study.

The XPS and SXPS data are consistent with the following picture (see Figure 16). At low exposures (i.e., < 30 L O_2), both XPS and SXPS can detect most of the oxide film since the film is probably ≤ 5 Å thick. The XPS and SXPS data for both Fe and Cr at low exposures are consistent with the presence of $\text{Fe}_{1+x}\text{Cr}_{2-x}\text{O}_4$ (with $0 \leq x \leq 0.4$; essentially FeCr_2O_4 , or iron chromite). Some FeO could also be present here for the higher R samples at these low exposures. During increasing O_2 exposure, the higher mobility of Fe results in the formation of an increasingly Fe-rich oxide film. Although there is certainly a greater Fe concentration towards the surface, there is no sharp boundary between Fe- and Cr-rich layers. In fact, the film might be described as a mixed oxide with a concentration gradient of Fe increasing towards the surface. The top 3 to 5 Å at the surface of the oxide film probably consists of $\text{Fe}_{1+x}\text{Cr}_{2-x}\text{O}_4$ with $x \geq 1$ in addition to Fe_2O_3 for the higher R samples. The observation of the disappearance of the LEED pattern as O_2 exposure is increased indicates that the $\text{Fe}_{1+x}\text{Cr}_{2-x}\text{O}_4$ or Fe_2O_3 phases do not exist in a crystalline form. Instead, an amorphous film exhibiting local atomic order similar to these crystalline phases exists. Presumably, O_2 exposures higher than those used in this study ($> 10,000$ L) would result in increasingly smaller amounts of Cr at the surface of the oxide film, resulting in an Fe-rich layer that consists primarily of Fe_2O_3 . This is supported by studies of the surface oxide films formed on Fe-Cr alloys¹² and high-Cr steels^{3,9} at room temperature.

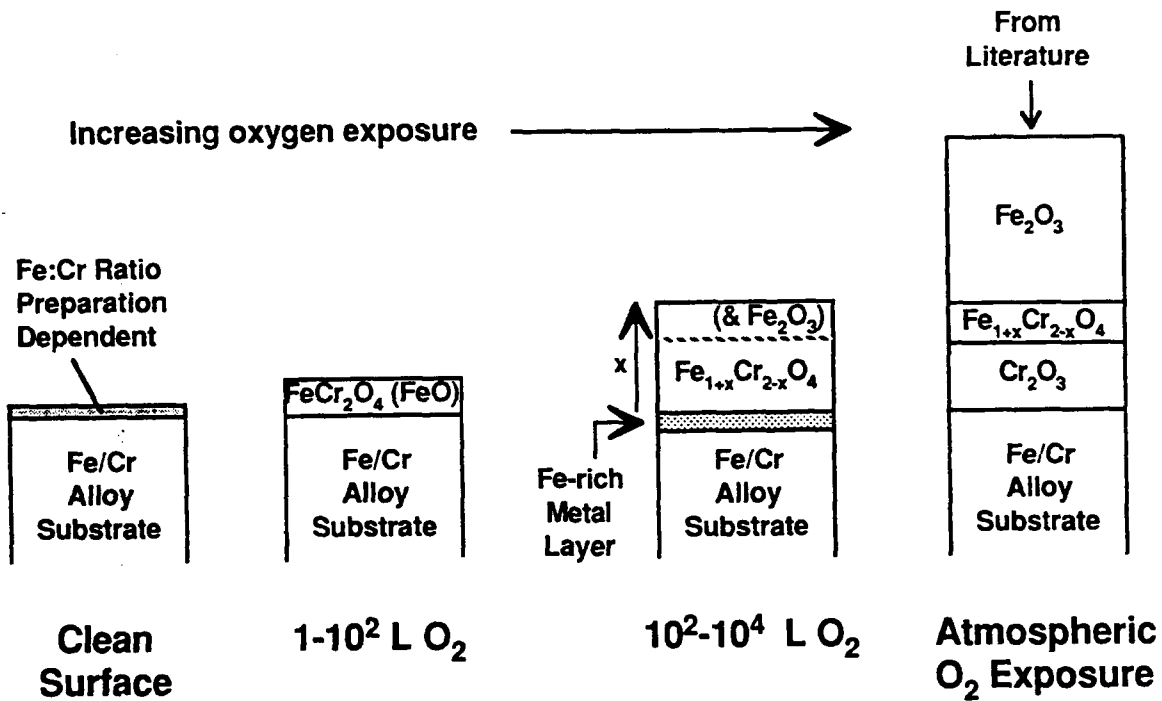


Figure 16. Schematic representation of results in this study on oxide film formation on the $\text{Fe}_{84}\text{Cr}_{16}(001)$ surface after exposure to O_2 ($\leq 10,000$ L O_2) at room temperature. In the schematic for 100 to 10^4 L O_2 , the arrow indicates increasing values of x in $\text{Fe}_{1+x}\text{Cr}_{2-x}\text{O}_4$ (due to greater amounts of Fe) toward the surface. The dotted line is applicable to the higher R samples, and indicates a possible boundary above which both Fe_2O_3 and $\text{Fe}_{1+x}\text{Cr}_{2-x}\text{O}_4$ are present. The current understanding of oxide films formed on the surfaces of Fe-Cr alloys and high-Cr steels exposed to atmospheric quantities of O_2 is also shown for comparison.

5. SUMMARY

A detailed study was conducted of the interaction of O_2 with the $Fe_{.84}Cr_{.16}$ (001) surface using variable photon energy photoelectron spectroscopy, including XPS ($h\nu = 1486.6$ eV), core-level SXPS ($h\nu = 130$ to 600 eV), and valence band SXPS ($h\nu = 150$ to 250 eV). We concentrated on relatively low O_2 exposures (1 to 10,000 L) and on room temperature substrates. A "qualitative depth profile" of the species present after oxidation was developed by taking advantage of the range of detected photoelectron kinetic energies. In general, our results indicate the formation of a mixed oxide film for these low exposures. It was found that the oxidation resistance of the $Fe_{.84}Cr_{.16}$ alloy was directly related to the extent of Cr segregation on its surface prior to oxidation.

The Cr concentration in the top few monolayers at the surface of the unoxidized $Fe_{.84}Cr_{.16}$ crystal could be controlled by varying the final anneal temperature reached after surface cleaning. The oxidation behaviors of surfaces with different initial Cr concentrations were similar, with the formation of similar phases and concentration gradients perpendicular to the surface. However, there were differences in the overall oxide thickness as shown by the attenuation of substrate core-level peaks with O_2 exposure for different surfaces. In addition, higher initial Cr concentrations on the unoxidized surface resulted in greater amounts of oxidized Cr present in the oxide film.

Small amounts of carbidic C remained on the unoxidized $Fe_{.84}Cr_{.16}$ (001) surfaces, simulating the surfaces of actual steels. Exposure of these surfaces to low exposures of O_2 (≤ 5 L) at room temperature resulted in virtual disappearance of the carbidic C, even for carbidic C quantities as high as one monolayer.

Initial oxidation resulted in oxide films that were richer in Cr than the unoxidized surface. The Fe:Cr ratios in the oxide films increased with increasing oxygen exposure, so that the oxide films became Fe-rich with respect to the initial surface for exposures of 2,000 to 10,000 L O_2 and higher, depending on the Fe:Cr ratio for the unoxidized surface. These higher exposures resulted in relatively Cr-rich oxides forming near the oxide/metal interface, and Fe-rich oxides forming near the surface of the growing film. The enhancement of Fe oxides near the surface of the films with increasing O_2 exposure is a result of the greater mobility of Fe atoms compared to Cr atoms, resulting in a transition from thermodynamic-controlled enhancement of Cr-oxides at low exposures to kinetic-controlled enhancement of Fe-oxides at higher exposures. However, Cr is still found to be present in the top few monolayers of the oxide film, even for exposures of 10,000 to 15,000 L O_2 , the highest exposures studied. This observation, along with comparison of core levels taken at different photoelectron kinetic energies (i.e., causing the positive slope of Figure 15 for O_2 exposures ≥ 400 L) supports the formation of mixed Fe-Cr-O species in the oxide films.

Chemical species identification was conducted by analysis of the shift in the oxide 2p and 3p core-level binding energies from that of the metallic component for both Fe and Cr. The changes in the shift of the oxide 2p and 3p core levels with increasing O_2 exposure were consistent with the formation of an Fe-Cr-O mixed oxide, probably with an amorphous $Fe_{1+x}Cr_{2-x}O_4$ -like structure. Specifically, initial O_2 exposure resulted in formation of a layer that exhibited XPS and SXPS binding energies consistent with amorphous $FeCr_2O_4$ (i.e., $FeO \cdot Cr_2O_3$), or

$\text{Fe}_{1+x}\text{Cr}_{2-x}\text{O}_4$ with $x \sim 0$) with some additional FeO (for the samples with higher Fe contents on their unoxidized surfaces). Longer exposures resulted in the surface of the films consisting of an Fe-rich $\text{Fe}_{1+x}\text{Cr}_{2-x}\text{O}_4$ -like species (i.e., with $x \geq 1$), along with Fe_2O_3 for samples with higher surface Fe contents.

The results of this work indicate some observations regarding the tribological behavior of steel bearings treated by lubricant additives.

- (1) We have shown here that differences in surface concentrations and resultant differences in oxidation behavior are controlled strongly by surface preparation procedures. Although high-Cr steels generally contain only ~ 15% Cr, we have shown that high temperatures can result in the top atomic layer consisting predominantly of Cr atoms. High temperatures are reached during the hardening process in steel manufacture. In addition, high surface temperatures can develop during wear of a bearing; the specific magnitude depends on the Hertzian stress, sliding speed, and sliding:rolling ratio. These varying temperatures could result in differences in the metallic Fe:Cr ratio at the worn bearing surface. This could affect the efficiency of the lubricant additive since, for example, PbNp was found to interact more strongly with low-Cr steel (i.e., 52100) rather than high-Cr steel (i.e., 440C)¹.
- (2) During wear of a bearing, the oxide film can be worn away, baring the metallic steel surface. PbNp breaks down to form a protective film of lead only when in contact with this metallic surface. However, our observation of a mixed $\text{Fe}_{1+x}\text{Cr}_{2-x}\text{O}_4$ oxide formation at the low O_2 exposures used in this study indicates that small amounts of similar species could form anew on worn surfaces in the low O_2 environment in space mechanisms. Therefore, care should be taken to minimize the amount of oxygen in these systems.

6. REFERENCES

- 1 S.V. Didziulis and P.D. Fleischauer, *Langmuir* **7** (1991) 2981.
- 2 S. Jin and A. Atrens, *Appl. Phys A* **50** (1990) 287.
- 3 J. Ferrante, NASA Tech. Note D-7789 (National Aeronautics and Space Administration, Washington, 1974).
- 4 S.C. Tjong, J. Eldridge, and R.W. Hoffman, *Appl. Surf. Sci.* **14** (1982-83) 297.
- 5 H.J. Mathieu and D. Landolt, *Corros. Sci.* **26** (1986) 547.
- 6 K. Nomura and Y. Ujihira, *J. Mat. Sci.* **25** (1990) 1745.
- 7 D.J. Young and D.F. Mitchell, *Oxid. Metals* **13** (1979) 437.
- 8 J.C. Hamilton, B.E. Mills, and R.E. Benner, *Appl. Phys. Lett.* **40** (1982) 499.
- 9 I. Olefjord, *Corros. Sci.* **15** (1975) 687.
- 10 C. Leygraf, G. Hultquist, and S. Ekelund, *Surf. Sci.* **51** (1975) 409.
- 11 M.J. Van Staden and J.P. Roux, *Appl. Surf. Sci.* **44** (1990) 263.
- 12 J.E. Castle, R. Ke, and J.F. Watts, *Corros. Sci.* **30** (1990) 771.
- 13 D.D. Wagman, W.H. Evans, V.B. Parker, R.H. Schumm, I. Halow, S.M. Bailey, K.L. Churney, and R.L. Nuttall, eds., *NBS Tables of Chemical Thermodynamic Properties* (AIP, NY, 1982); in *J. Phys. Chem. Ref. Data* **11** (suppl. 2).
- 14 G.C. Allen, S.J. Harris, J.A. Jutson, and J.M. Dyke, *Appl. Surf. Sci.* **37** (1989) 111.
- 15 G.C. Allen, J.M. Dyke, S.J. Harris, and A. Morris, *Oxid. Metals* **29** (1988) 391.
- 16 L.V. Pavlinov, E.A. Isadzanov, and U.P. Smirnov, *Fiz. Metal Metalloved.* **25** (1968) 959.
- 17 F.P. Fehlner and N.F. Mott, *Oxid. Metals* **2** (1970) 59.
- 18 C. Uebing, *Surf. Sci.* **225** (1990) 97.
- 19 J.H. Scofield, *J. Electron Spectrosc. Relat. Phenom.* **8** (1976) 129.
- 20 S. Tanuma, C.J. Powell, and D.R. Penn, *Surf. Sci.* **192** (1987) L849.
- 21 M.P. Seah and W.A. Dench, *SIA, Surf. Interf. Anal.* **1** (1979) 2.
- 22 D.E. Eastman, J.J. Donelon, N.C. Hien, and F.J. Himpsel, *Nucl. Instrum. Methods* **172**, (1980) 327 .

- 23 F.J. Himpsel, Y. Jugnet, D.E. Eastman, J.J. Donelon, D. Grimm, G. Landgren, A. Marx, J.F. Morar, C. Oden, and R.A. Pollak, *Nucl. Instrum. Methods* **222**, 107 (1984).
- 24 J.R. Lince, T.B. Stewart, M.M. Hills, P.D. Fleischauer, J.A. Yarmoff, and A. Taleb-Ibrahimi, *Surf. Sci.* **210**, 387 (1989).
- 25 J.J. Yeh and I. Lindau, **32** (1985) 1.
- 26 B.L. Maschhoff and N.R. Armstrong, **7** (1991) 693.
- 27 C.D. Wagner, W.M. Riggs, L.E. Davis, J.F. Moulder, and G.E. Muilenberg, *Handbook of X-ray Photoelectron Spectroscopy* (Perkin-Elmer Corp., Physical Electronics Div., Eden-Prairie, MN, 1979).
- 28 E. Desimoni, C. Malitesta, P.G. Zambonin, and J.C. Riviére, *Surf. Interf. Anal.* **13** (1988) 173.
- 29 G.C. Allen, P.M. Tucker, and R.K. Wild, *J. Chem. Soc. Faraday Trans. II* **74** (1978) 1126.
- 30 D. Shuttleworth, *J. Phys. Chem.* **84** (1980) 1629.
- 31 R. Merryfield, M. McDaniel, and G. Parks, *J. Catal.* **77** (1982) 348.
- 32 N.S. McIntyre and D.G. Zetaruk, *Anal. Chem.* **49** (1977) 1521.
- 33 V.V. Nemoshalenko, V.V. Didyk, V.P. Krivitskii, and A.I. Senekevich, *Zh. Neorg. Khim.* **28** (1983) 2182.
- 34 G.C. Allen, M.T. Curtis, A.J. Hooper, and P.M. Tucker, *J. Chem. Soc. Dalton Trans.* (1974) 1525.
- 35 D. Brion, *Appl. Surf. Sci.* **5** (1980) 133.
- 36 H. Konno and M. Nagayama, *J. Electron Spec. Relat. Phenom.* **18** (1980) 341.
- 37 P.A. Dowben, M. Grunze, and D. Wright, *Surf. Sci.* **134** (1983) L524.
- 38 L. Ramqvist, K. Hamrin, G. Johansson, A. Fahlman, and C. Nordling, *J. Phys. Chem. Solids* **30** (1969) 1835.
- 39 M.F. Ebel, *Surf. Interf. Anal.* **3** (1981) 149.
- 40 J. R. Lince, S. V. Didziulis, D. K. Shuh, T. D. Durbin, and J. A. Yarmoff, to be published.
- 41 C.R. Brundle, T.J. Chuang, and K. Wandelt, *Surf. Sci.* **68** (1977) 459.
- 42 R.O. Ansell, T. Dickinson, and A.F. Povey, *Corros. Sci.* **18** (1978) 245.
- 43 D.E. Eastman and J.L. Freeouf, *Phys. Rev. Lett.* **34** (1975) 395.
- 44 P. Mills and J.L. Sullivan, *J. Phys. D* **16** (1983) 723.

- 45 F.J. Himpsel, F.R. McFeely, A. Taleb-Ibrahimi, and J.A. Yarmoff, *Phys. Rev. B* **38** (1988) 6084.
- 46 *NIST X-ray Photoelectron Spectroscopy Database, Version 1.0*, compiled by C. D. Wagner; NIST Standard Reference Database 20 (Standard Reference Data, NIST, Gaithersburg, MD, 20899).
- 47 A.D. Pelton, H. Schmalzreid, and J. Sticher, *J. Phys. Chem. Solids* **40** (1979) 1103.

TECHNOLOGY OPERATIONS

The Aerospace Corporation functions as an "architect-engineer" for national security programs, specializing in advanced military space systems. The Corporation's Technology Operations supports the effective and timely development and operation of national security systems through scientific research and the application of advanced technology. Vital to the success of the Corporation is the technical staff's wide-ranging expertise and its ability to stay abreast of new technological developments and program support issues associated with rapidly evolving space systems. Contributing capabilities are provided by these individual Technology Centers:

Electronics Technology Center: Microelectronics, solid-state device physics, VLSI reliability, compound semiconductors, radiation hardening, data storage technologies, infrared detector devices and testing; electro-optics, quantum electronics, solid-state lasers, optical propagation and communications; cw and pulsed chemical laser development, optical resonators, beam control, atmospheric propagation, and laser effects and countermeasures; atomic frequency standards, applied laser spectroscopy, laser chemistry, laser optoelectronics, phase conjugation and coherent imaging, solar cell physics, battery electrochemistry, battery testing and evaluation.

Mechanics and Materials Technology Center: Evaluation and characterization of new materials: metals, alloys, ceramics, polymers and their composites, and new forms of carbon; development and analysis of thin films and deposition techniques; nondestructive evaluation, component failure analysis and reliability; fracture mechanics and stress corrosion; development and evaluation of hardened components; analysis and evaluation of materials at cryogenic and elevated temperatures; launch vehicle and reentry fluid mechanics, heat transfer and flight dynamics; chemical and electric propulsion; spacecraft structural mechanics, spacecraft survivability and vulnerability assessment; contamination, thermal and structural control; high temperature thermomechanics, gas kinetics and radiation; lubrication and surface phenomena.

Space and Environment Technology Center: Magnetospheric, auroral and cosmic ray physics, wave-particle interactions, magnetospheric plasma waves; atmospheric and ionospheric physics, density and composition of the upper atmosphere, remote sensing using atmospheric radiation; solar physics, infrared astronomy, infrared signature analysis; effects of solar activity, magnetic storms and nuclear explosions on the earth's atmosphere, ionosphere and magnetosphere; effects of electromagnetic and particulate radiations on space systems; space instrumentation; propellant chemistry, chemical dynamics, environmental chemistry, trace detection; atmospheric chemical reactions, atmospheric optics, light scattering, state-specific chemical reactions and radiative signatures of missile plumes, and sensor out-of-field-of-view rejection.